Strain mapping of semiconductor specimens with nm-scale resolution in a transmission electron microscope

David Cooper [a],[*], Thibaud Denneulin [a], Nicolas Bernier [a], Armand Béché [b], Jean-Luc Rouvière [b]

[a] Univ. Grenoble Alpes, F-38000 Grenoble, France and CEA, LETI, MINATEC Campus, F-38054 Grenoble, France
[b] Univ. Grenoble Alpes, F-38000 Grenoble, France and CEA, INAC, MINATEC Campus, F-38054 Grenoble, France

ABSTRACT

The last few years have seen a great deal of progress in the development of transmission electron microscopy based techniques for strain mapping. New techniques have appeared such as dark field electron holography and nanobeam diffraction and better known ones such as geometrical phase analysis have been improved by using aberration corrected ultra-stable modern electron microscopes. In this paper we apply dark field electron holography, the geometrical phase analysis of high angle annular dark field scanning transmission electron microscopy images, nanobeam diffraction and precession diffraction, all performed at the state-of-the-art to five different types of semiconductor samples. These include a simple calibration structure comprising 10-nm-thick SiGe layers to benchmark the techniques. A SiGe recessed source and drain device has been examined in order to test their capabilities on 2D structures. Devices that have been strained using a nitride stressor have been examined to test the sensitivity of the different techniques when applied to systems containing low values of deformation. To test the techniques on modern semiconductors, an electrically tested device grown on a SOI wafer has been examined. Finally a GaN/AlN superlattice was tested in order to assess the different methods of measuring deformation on specimens that do not have a perfect crystalline structure. The different deformation mapping techniques have been compared to one another and the strengths and weaknesses of each are discussed.

© 2015 The Authors. Published by Elsevier Ltd. This is an open access article under the CC BY-NC-ND license (http://creativecommons.org/licenses/by-nc-nd/4.0/).

1. Introduction

Strain is used widely in the semiconductor industry to improve the performance of micro electronic devices (Chu et al., 2009) or to tune properties of opto-electronics devices, such as the frequency of the emitted photons (Stier et al., 1999) and to modify the properties of ferroics (Schlom et al., 2007; Catalan et al., 2012). In order to better understand and improve the properties of these devices, it is important to have accurate information about the strain fields that are present. There are many different methods that can be used to measure strain in semiconductors. X-ray diffraction (Miao et al., 1999) and micro-Raman Spectroscopy (Senez et al., 2003) are very well established techniques which now can be used with spatial resolutions that are approaching tens of nanometers. For improved spatial resolution, transmission electron microscopy (TEM) based techniques such as Moire interference (Sands, 1987), convergent beam electron diffraction (CBED) (Armigliato et al., 2003, 2008;

Kim et al., 2004; Huang et al., 2006; Zhang et al., 2006; Diercks et al., 2011) and strain mapping from either real space analysis (Jouneau et al., 1994; Seitz et al., 1995; Rosenauer et al., 1997a,b) or the geometrical phase analysis (GPA) (Hytch et al., 1998; Rouvière and Sarigiannidou, 2006) of high resolution TEM images, have been used to provide information about the strain in semiconductor devices for more than 20 years

In the last five years there has been a lot of activity in the development of metrology for strain mapping which has been driven by the needs of semiconductor research. Many new techniques such as dark field electron holography (DFEH) (Hytch et al., 2008) and in-line dark field holography (Koch et al., 2010b) have been developed and older techniques such as diffraction and GPA have been improved, such as by the use of aberration correction (Hue et al., 2008b). In this paper we will focus on four different deformation mapping techniques and show how they have been applied to five different types of semiconductor samples. The techniques have been selected on the basis that they can provide information about strain without having to use complicated data processing and are compatible with focused ion beam (FIB) milling which is needed to provide the site-specificity for semiconductor metrology. The

techniques used are DFEH, the GPA of images that have been acquired by high angle annular dark field imaging (HAADF STEM), nanobeam diffraction (NBED) and precession electron diffraction (N-PED).

The structure of this paper is to briefly introduce each technique as applied to a simple calibration specimen. We will then present four different specimens that each have different problems experimentally and examine these specimens using each technique. All of the specimen preparation, experiments and data analysis that are presented in this paper has been performed by the same person which allows an objective assessment of the strengths and weaknesses of the different techniques.

1.1. Experimental procedure

The experiments referred to in this paper were performed over a 5 year time period. Due to the reproducible nature of FIB sample preparation it is reasonably straightforward to keep the experimental procedure consistent. All of the DFEH and NBED experiments were performed using a first generation, probe-corrected FEI Titan equipped with three condenser lenses, an electron biprism and a dedicated lens for Lorentz microscopy. All of the HAADF STEM and N-PED experiments were performed on a double-aberration corrected FEI Titan Ultimate equipped with an X-FEG, monochromator, three condenser lenses, Digiscan and an electron biprism. For recording the information on the CCD, a 2048^2 pixel camera was used, however in general, the acquisitions were double binned such that the pixels are read out in blocks of 2×2, and thus 1024^2 pixel images are recorded to either speed up the acquisition readout or to increase the number of electrons recorded in each data point by a factor of 4.

For the diffraction patterns acquired during the NBED experiments it was complicated to acquire deformation maps as when the experiments were performed, it was not possible to save the images individually. The data was saved in one file, thus the size of the map was limited by the memory of Windows XP. Therefore for the experiments described here, NBED has only been used to acquire strain profiles. The N-PED data has been acquired using home made Digital Micrograph scripts where each diffraction pattern is saved individually and thus deformation maps of unlimited size are possible. The NBED experiments could have been repeated using this new acquisition system, however we have not done this and in this work, the NBED is only used for deformation profiles and N-PED for maps. All of the data acquired using all of the different techniques has been processed using software written at CEA.

All experiments shown here have been performed at 200 kV to limit the damage to the silicon specimens which are the basis for most semiconductor research at CEA LETI. For example, for NBED and N-PED, the spatial resolution can be improved by operating the microscope at 300 kV, however in order to simplify the paper this has not been done. For DFEH this is more complicated, more electrons will be transmitted at 300 kV, but they will interact less with the specimen. For HAADF STEM, the spatial resolution will be improved at 300 kV. Where appropriate the effects of changing the operating voltage of the microscope have been discussed.

For TEM based measurement techniques, it is the relative deformation between a nominally unstrained reference (usually the substrate) and a region of interest that is measured. This is known as Lagrange deformation, ε_L where d^{obj} is the lattice parameter for the strained material of interest and d^{ref} the reference lattice parameter;

$$\varepsilon_L = \frac{d^{obj} - d^{ref}}{d^{ref}}. \tag{1}$$

In terms of the notation, in all cases the z-direction refers to the growth direction which refers unless otherwise stated to the

Table 1
Different specimens examined in this work and difficulties encountered.

Sample type	Information required and difficulties
SiGe calibration specimen	10-nm-thick layers
	Good spatial resolution in 1 dimension required
Conventional bulk semiconductor device	2D structure, spatial resolution required in both directions
	Precision to measure deformation without averaging
Nitride stressor	2D structure, spatial resolution required in both directions
	Low values of deformation are expected
Silicon on insulator device	Very small regions of interest (2–10 nm)
	Mis-orientation between region of interest and reference
AlN/GaN superlattice	Large values of deformation
	High density of defects and dislocations

deformation of the $(0\,0\,1)$ lattice planes for silicon (ϵ_z). The x direction is in all cases the in-plane direction and refers to unless otherwise stated to the deformation of the $(1\,1\,0)$ planes (ϵ_x).

1.2. Specimens and specimen preparation

In order to illustrate the strengths and weaknesses of each technique, we have applied them to five different types of specimens. Table 1 shows a summary of the different types of specimens and the requirements and difficulties which are expected to be encountered for each.

(1) A simple calibration specimen comprised of 10-nm-thick SiGe layers grown in Si by epitaxy. Here there are no unknown parameters for the simulations of the deformation and thus this can be used to assess the accuracy of each technique. This is the most simple type of specimen that can be examined and a high precision in the measurement is not required as averaging over a large area can be used.
(2) A silicon recessed SiGe source and drain test device with 35-nm-gate has been examined. Here good spatial resolution is required in two different directions and averaging of the measured deformation is limited by the size of the device.
(3) A silicon 28-nm technology, high-k metal gate nMOS device specimen stressed using a nitride film was examined to assess the ability of the different techniques for the measurement of low values of deformation.
(4) A silicon pMOS device grown on SOI were examined to assess the suitability of each technique for specimens when the reference does not have the same orientation as the region of interest. An additional complication for these specimens are their small dimensions with regions of interest where the deformation must be measured of less than 10 nm.
(5) An AlN/GaN superlattice has been examined to illustrate the problems encountered when measuring the deformation in specimens with non-perfect crystal quality.

The calibration specimen was designed so that the different deformation mapping techniques could be tested and easily compared to simulations to account for the relaxation of the thin TEM specimen and assess the accuracy of the measurements (Béché et al., 2013). Fig. 1(a) shows the calibration specimen that was examined which was grown using reduced pressure chemical vapour deposition (RPCVD) and comprised from top to bottom, a 150-nm-thick capping layer, then four 10-nm-thick SiGe layers with Ge concentrations of 45%, 38%, 31% and 20%, each separated by 30 nm of silicon on a silicon substrate. The principle of the calibration specimen is shown in Fig. 1(b). As the growth is epitaxial, the lattice spacing for the in-plane (x-direction) does not
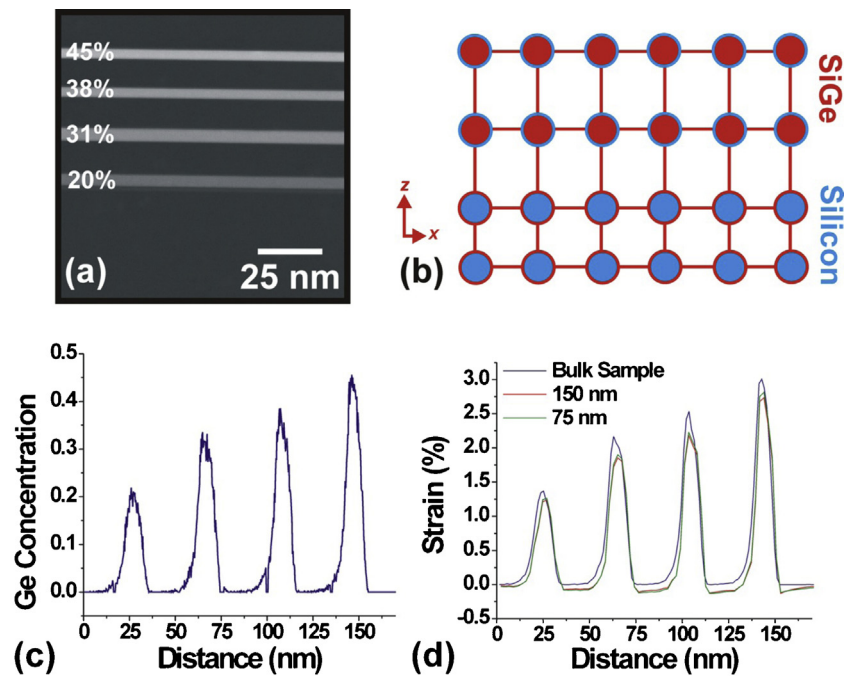
Fig. 1. (a) HAADF STEM image of the calibration specimen used for these experiments. (b) Schematic showing the relaxation in the *z*-direction and effect of the expanded lattice parameter for specimens grown in epitaxy. (c) SIMS profiles showing the Ge concentration in the specimen. (d) Finite element simulations showing the expected strain for the growth or *z*-direction for an infinitely thick (bulk) specimen and in a TEM specimen with thicknesses of 75 and 150 nm.

change. However, for the growth (*z*-direction) the lattice parameter is expanded due to the presence of Ge and it is this expansion relative to the silicon that is measured. Fig. 1(c) shows a secondary ion mass spectrometry (SIMS) profile of the calibration specimen revealing the Ge concentrations in the different layers. The information from the SIMS profile was used in the finite element (FE) simulations in Comsol Multiphysics modelling software which provides a calculation of the deformation that would be expected in the thin TEM specimens. Fig. 1(d) shows the results from the FE-simulations for an infinitely thick bulk-type specimen and for TEM specimens of thickness 75 and 150 nm. The deformation in the layers has been reduced by approximately 10% in the TEM specimens compared to what would be expected in the bulk wafer. This result demonstrates that the relaxation of the TEM specimens does affect the measured strains and without the use of simulations it is not possible to determine accurate values. However, there is only a small difference between the strain expected for the 75 and 150 nm thick TEM specimens. This is a positive result as it is relatively easy to prepare specimens for examination within this range of thicknesses and thus comparative studies between similar types of devices are possible.

For all of the experiments discussed in this manuscript, the specimens were prepared using FIB-milling. This approach is indispensable in the semiconductor industry where large quantities of specimens need to be prepared from precise locations on a wafer. The regions of interest are located using a scanning electron microscope (SEM) and then protected using 2–3 μm of platinum using ion beam assisted deposition (IBAD) in the FIB to protect the specimen from the tails of the ion beam. The specimens are then attached to a TEM grid using in situ lift-out and thinned to around 500 nm using a conventional 30 kV operation voltage at a medium current of around 1 nA. The specimens are finished using a low beam energy in the range 5–8 kV to provide a compromise between the reduction of the surface damage and the ability to provide a finished specimen with parallel sides. For a parallel-sided membrane, the specimen is tilted into the beam by 2°. The final

specimen thicknesses can easily be controlled to be in the range 100–150 nm. When regions close to the surfaces of the specimens are examined, a thin layer of marker pen is written onto the specimen surface over the region of interest and then a protective Pt layer is deposited on top using ion beam assisted deposition in the FIB. The specimens are then plasma cleaned in order to remove the ink and leave a region of vacuum near the region of interest such that the protective layers do not interfere with the intrinsic strain that is present in the device. For deformation mapping the specimen should not be too thin (>100 nm) to limit the effects of thin foil relaxation, and more importantly to prevent specimen bending (Gibson and Treacy, 1984; Clement et al., 2004; Rosenauer et al., 2006; Houdellier et al., 2008). However, the effects of specimen relaxation are strongly dependent on the geometry of the sample and the strain component measured.

2. Introducing the techniques

2.1. Dark field electron holography

DFEH is a variation of off-axis electron holography which was first demonstrated in 1986 (Hanszen, 1986) and then for the measurement of strain in semiconductor devices in 2008 (Hytch et al., 2008; Lubk et al., 2014). DFEH is now used in the semiconductor industry to perform systematic materials studies (Hue et al., 2008a, 2009; Gouyé et al., 2009; Hytch et al., 2011; Denneulin et al., 2012, 2014; Wang et al., 2013; Cherkashin et al., 2013; Reboh et al., 2013a,b; Cooper et al., 2014a,b). Off-axis electron holography is a well established technique that has been used for many years to study magnetic and electrostatic potentials (Tonomura, 1987; Lichte et al., 2008; McCartney and Smith, 2008). An electron biprism is used to interfere an object and reference electron wave to provide an interference pattern which is also known as a hologram. The phase of the electrons can be obtained from the shifts in the hologram fringes. Following the notation used by Hytch, the
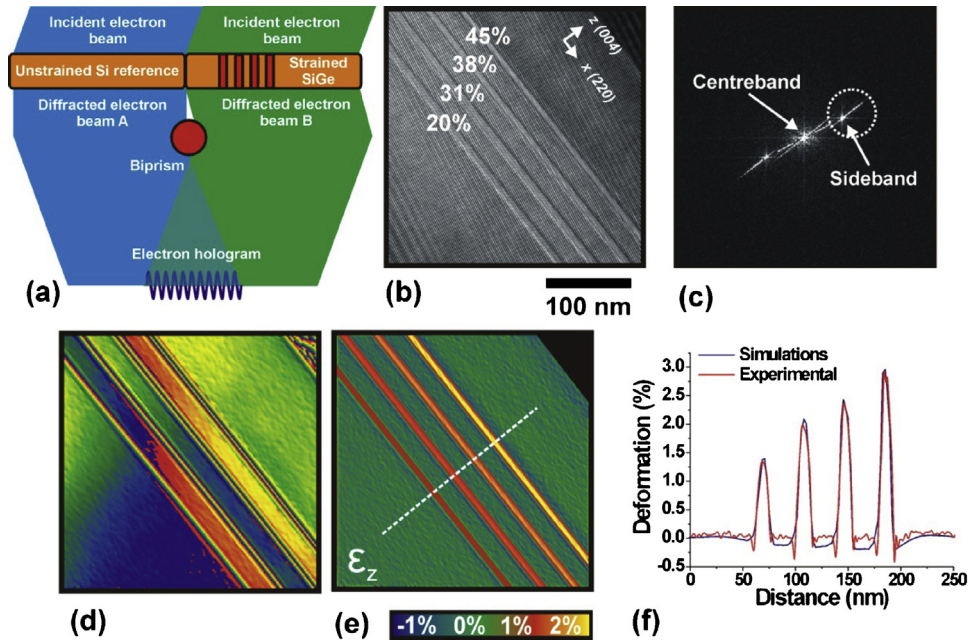
Fig. 2. (a) Schematic of the DFEH setup. (b) Dark field electron hologram of the calibration specimen acquired using a 0 0 4 diffracted beam, (c) a Fourier transform of (b). (d) The reconstructed phase image and (e) ϵ_z deformation map. (f) Strain profile extracted from the dashed line in (e) compared to finite element simulations.

phase, $\phi_g(r)$, where r is the position vector can be written as having four components,

$$\phi_g(r) = \phi_g^G(r) + \phi_g^C(r) + \phi_g^E(r) + \phi_g^M(r) \qquad (2)$$

where $\phi_g^G(r)$ is the geometrical phase that describes the distortion a the crystal lattice, $\phi_g^C(r)$ is the crystal phase which results from the scattering of electrons from the crystal potential, $\phi_g^E(r)$ is the contribution of electrical fields in and around the specimen and $\phi_g^M(r)$ is the magnetic contribution (Hytch et al., 2008). Therefore, as DFEH exploits the phase of the electrons, care must be taken when examining devices where there is a varying electrostatic potential due to either changes in composition (mean inner potential) or where specimens are strongly doped as this may be interpreted as strain when applying a GPA algorithm.

DFEH was applied to the calibration specimen and Fig. 2(a) shows a schematic of the experiment. The reference wave passes through the unstrained substrate and is interfered with the object wave which passes through the strained region of interest. The specimen is tilted to a two-beam condition and electrons that have been diffracted from the lattice planes of interest are selected by using an objective aperture. Here, the (0 0 4) beam is selected in order to assess the lattice expansion in the growth direction. Fig. 2(b) shows the obtained hologram with a fringe spacing of 2 nm. In order to increase the signal-to-noise in the calculated strain map, a long exposure time of 64 s has been used (Cooper et al., 2008, 2009). Fig. 2(c) shows a FFT of the hologram. The information about the deformation is encoded in the sideband, which is selected and an inverse Fourier transform is applied to provide a complex image, from which a phase and amplitude image can be calculated. The phase image shown in Fig. 2(d) corresponds to the displacement field for the selected lattice planes and a strain map can then be calculated using a GPA algorithm (Hytch et al., 1998; Rouvière and Sarigiannidou, 2006), where the derivative of the phase, ϕ_{GPA} gives directly the difference in the wave vectors of the strained region of interest, $\mathbf{g}_{obj}$ and the reference, $\mathbf{g}_{ref}$,

$$\nabla_{\mathbf{r}} \phi_{GPA} = 2\pi \Delta \mathbf{g} = 2\pi (\mathbf{g}_{obj} - \mathbf{g}_{ref}) \qquad (3)$$

Therefore in one dimension, the strain can be measured with respect to the reference interplanar distance where $d_{ref} = 1/\mathbf{g}_{ref}$ and $d_{obj} = 1/\mathbf{g}_{obj}$. The Lagrange deformation, ε_L is then obtained by substituting these values into Eq. (1). Fig. 2(e) shows the strain map obtained for the calibration specimen. The lattice expansion in the SiGe relative to the substrate region can be seen in the layers. The specimen thickness was measured by CBED and found to be 77 nm. Fig. 2(f) shows the simulations compared to the experimental results extracted from the indicated region in (e) demonstrating that the measurement made by DFEH is in agreement to what is expected from the simulations. The experimental profile has been extracted from across a width of 3.6 nm which corresponds to 10 pixels in the deformation map.

The spatial resolution of DFEH is determined by the fringe spacing of the interference pattern. In principle the position of one fringe will provide a data point in the reconstructed phase image which corresponds to the deformation map. However, the presence of the conventional intensity image which is superimposed on the recorded hologram restricts the spatial resolution to 3 times the fringe spacing when applying a mask in Fourier space (Leith and Upatnieks, 1962). Ultimately it is the coherence of the electron beam which limits the fringe spacing that can be achieved. However, when using appropriate lens settings in modern electron microscopes, for the fields of view that are typically required for today's semiconductor devices, the sampling of the fringes on the finite CCD camera will also limit the spatial resolution. Assuming that 6 pixels are needed to accurately record the position of an individual interference fringe and using a 2048 pixel camera to record a field of view of 300 nm², 1 nm spaced fringes can be recorded to provide a spatial resolution of around 3 nm. Even if very fine fringe spacings can be obtained, an additional constraint is that DFEH is usually performed in Lorentz mode and the aberrations in this lens limit the achievable spatial resolution to around 2.5 nm. Due to experimental constraints regarding the coherence of the electron beam, the modulation transfer function (MTF) of the CCD camera and the need to obtain electron holograms with sufficient counts and contrast, the majority of papers on the subject tend to use fringe spacings around 2 nm and as a consequence, most reported results found in the literature obtained by DFEH report spatial report
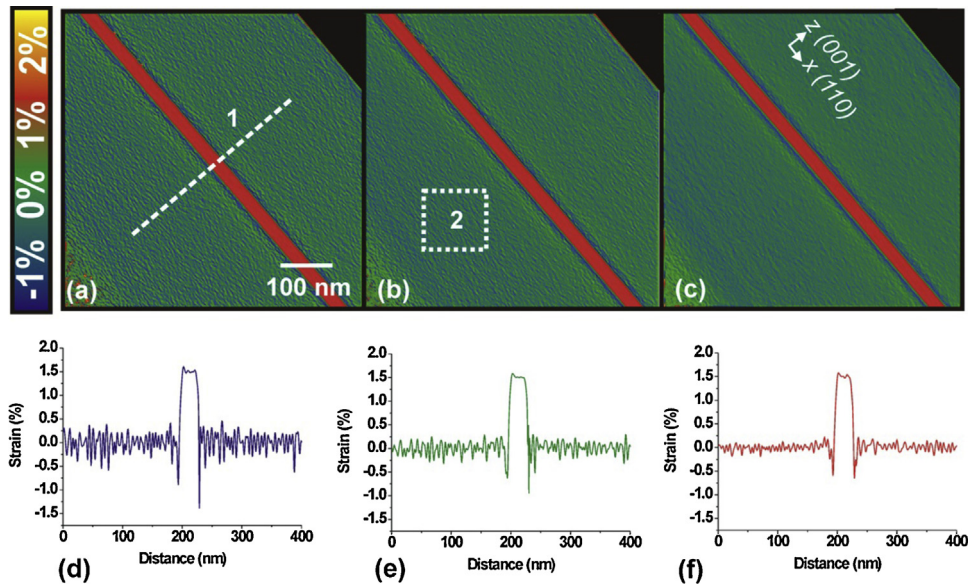
Fig. 3. (a)–(c) ϵ_z Deformation maps for a single 30 nm-thick Si$_{0.70}$Ge$_{0.30}$ layer grown by epitaxy obtained from holograms acquired for 4, 16 and 64 s respectively. (d)–(f) Deformation profiles extracted from (a)–(c) respectively.

resolutions in the range 4–6 nm (Hytch et al., 2008; Cooper et al., 2009, 2014a). An additional and important constraint on the spatial resolution that is obtainable when using DFEH is the specimen tilt. In order to obtain a dark field hologram, the specimen is tilted to a two beam condition which means that the specimen is tilted from a zone axis by typically 1–2°. For a 100-nm-thick specimen, a tilt of 2° will correspond to a blurring of the specimen in projection of 3.5 nm.

The signal to noise ratio is more difficult to define for DFEH as the technique is extremely dependent on the roughness, flatness and thickness of the specimen and these are typically the limiting factors. In the most simple case of conventional electron holography, the noise in the reconstructed phase image $\delta\phi$, is given by;

$$\delta\phi = \frac{2\pi}{\mu\sqrt{N}} \qquad (4)$$

where μ is the contrast of the electron hologram and N is the number of electron counts in the reconstructed phase image (Harscher and Lichte, 1986). Thus for optimum precision in the measurement of the deformation, electron holograms need to be acquired for the optimum amount of time before instabilities in the microscope reduce the hologram contrast and specimen drift impacts the spatial resolution. For most electron microscopes, the optimum acquisition time is between 8 and 16 s, however for the latest generation of ultra-stable electron microscopes, electron holograms of 60 s or more can be obtained whilst maintaining excellent fringe contrast which have the effect using the whole dynamic range of the CCD camera (Cooper et al., 2008).

An experimental example of the obtainable precision is best performed using a simple specimen. Fig. 3 shows ϵ_z deformation maps for a 100-nm-thick silicon specimen with a single 30 nm-thick Si$_{0.70}$Ge$_{0.30}$ layer grown by epitaxy. In Fig. 3(a)–(c) deformation maps which are obtained for electron holograms acquired for 4, 16 and 64 s respectively are shown. The deformation profiles acquired from the region indicated A are shown in Fig. 3(d)–(f) and the improvement in the signal to noise ratio can be observed as the hologram acquisition time period is increased. To give a idea of the precision that is obtainable, the standard deviation in the unstrained silicon substrate has been measured from the region indicated by B. Here values of ±0.2%, 0.1% and 0.05% have been obtained for the holograms acquired for 4, 16 and 64 s respectively

which follows the law shown in equation 4 as the hologram contrast was constant in all of the acquired holograms. Sensitivities of better than ±0.02% have been demonstrated in well prepared and perfect epitaxially grown specimens. The measured precision of the deformation measurement is affected by the specimen thickness. Systematic studies of the specimen discussed in Fig. 3 have shown that the noise observed in a 180-nm-thick specimen doubled compared to a 100-nm-thick specimen (Cooper et al., 2009).

Experimental DFEH can also be difficult to learn and perform. An additional problem for FEI microscopes operated in Lorentz mode in dark field mode is that although it is possible to tilt the electron beam to position the (2 2 0) spot on the optical axis to measure the ϵ_x deformation, there is not enough beam tilt to use the (0 0 4) diffracted beam for ϵ_z. Different approaches such as using two different (1 1 1) beams to obtain ϵ_x and ϵ_z can be used, although here it is difficult to superimpose the different phase images due to the specimen tilts that are required to obtain a two beam condition. An alternative is to use the microscope in dual lens mode (Wang et al., 2004, 2015), where the extra beam tilt that is needed can be obtained by lightly exciting the objective lens.

The new generations of ultra-stable electron microscopes make DFEH more straightforward to perform, the use of high brightness electron guns and cold FEGs allow holograms with more counts or higher contrast to be acquired for a given acquisition time. It is also straightforward to add many electron holograms together to obtain phase images with phase resolutions as good as $2\pi/2000$ (Voelkl and Tang, 2010; McLeod et al., 2014). Dedicated multi-biprism electron microscopes such as the Hitachi iTEM at CEMES in Toulouse make dark field electron holography a much more versatile technique in terms of the obtainable spatial resolution and field of view. The improvements in instrumentation and data processing mean that the principal limitations of DFEH are not only microscope dependent. The phase of an electron is very sensitive to the changes in specimen thickness, thus the specimen needs to be perfectly flat. The specimen requires a reference region which is the same size as the region of interest to be nearby and have the same orientation as the region of interest which is not always the case. Most importantly the specimen tilt required to obtain a two-beam condition limits the spatial resolution that can be obtained which is critical for state-of-the-art semiconductor devices.
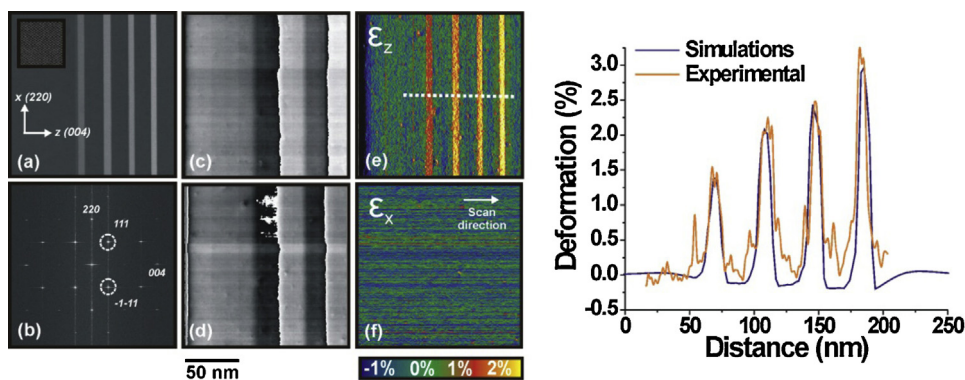
Fig. 4. (a) A 4k × 4k HAADF STEM image with inset showing the sampling of the atoms. (b) Fourier transform of (a) showing the principal component frequencies of the image from which the phase images in (c) and (d) can be calculated from which the deformation maps for (e) ϵ_z and (f) ϵ_x can be determined. (g) The extracted ϵ_z profile acquired from the region indicated by the dashed line in (e) compared to simulations.

2.2. Deformation mapping from high-resolution images

GPA has been used for more than 15 years as a way to recover the strain from high-resolution TEM images (Hytch et al., 1998; Hytch and Plamann, 2001; Takeguchi et al., 2004; Rouvière and Sarigiannidou, 2006; Johnson et al., 2007). This method is best adapted for small specimens such as quantum dots (Sarigiannidou et al. 2005) as the need to sample each atomic column correctly leads to a small field of view for most CCD cameras. In addition, high-resolution TEM is very sensitive to specimen preparation and changes in thickness can lead to contrast reversal introducing artefacts in the deformation maps, especially when large fields of views are desired. HAADF STEM uses an annular detector to record the electrons that are scattered to an angle depending on the Z-number of the atoms in the atomic columns and as such their positions can be directly interpreted. The stability of the latest generation electron microscopes now allow GPA algorithms to be applied to images acquired by HAADF STEM (Chung et al., 2010; Hosseini-Vargargah et al. 2011; Cooper et al., 2012b). In addition, the ability to acquire images with 4k by 4k or even 8k by 8k pixels means that relatively large fields of view up to a few hundreds of nanometers can now be obtained in a single image. Fig. 4 shows the procedure used for strain mapping (a) a HAADF image is acquired then (b) a Fourier transform is applied and the spots containing the information about the lattice planes of interest are selected. In this case the {1 1 1} families of spots are the most intense and are used to provide maps with the best signal to noise ratio and these are used to calculate a geometrical phase image from which the deformation maps for ϵ_x, ϵ_{xz} and ϵ_z directions. Unlike for DFEH, the HAADF images are taken on a zone axis so there are no problems with the correction of specimen tilts and beam alignments when combining phase images from different spots in the FFT. Deformation maps could also be obtained by selecting only one spot in the FFT such as the (0 0 4) for the growth direction however this approach leads to poorer signal to noise ratio. Fig. 4(e) shows the deformation map calculated for the growth direction and (f) for the in-plane direction. The direction of the fast scan has been chosen such that it is in the same direction as the direction of the deformation that is being measured. In this case it is in the same direction as the growth direction. This minimises the artefacts that are introduced as the scan moves from the end of one row to the beginning of the next, known as the slow-scan direction which can be observed as the horizontal lines that are present in the ϵ_x map shown in Fig. 4(f). These distortions which are discussed in more detail elsewhere (Jones and Nellist, 2013) could also be removed during data processing (Braidy et al., 2012).

One of the advantages of using HAADF STEM for strain mapping is that it is very insensitive to experimental settings or specimen preparation. To illustrate this, HAADF STEM images were acquired

of a unstrained silicon specimen oriented on the [1 1 0] zone axis with regions of different thicknesses. The images were recorded using a 4096 pixel^2 acquisition with a total field of view of 110 nm^2 and the deformation maps were calculated using a mask in Fourier space to provide a spatial resolution of 3 nm. Fig. 5(a) shows a 10 nm^2 detail from a 125 nm^2 HAADF STEM image of a 157-nm-thick specimen and (b) the corresponding ϵ_x deformation map. Fig. 5(c) shows a detail of a HAADF image and (d) ϵ_x for a 184-nm-thick specimen. Finally, Fig. 5(e) shows a detail of a HAADF image and (f) ϵ_x for a 286-nm-thick specimen. The standard deviation has been measured in the region indicated and is found to be ±0.36% for all of the different specimen thicknesses which is an order of magnitude worse than can be achieved by DFEH. The vertical lines which are present in the deformation maps are from 50 Hz noise in the room which although are seen in the maps, are not visible in the HAADF STEM images.

Fig. 5(g)–(l) shows the effect of sampling on the signal to noise ratio measured in the deformation maps. Maps of ϵ_x are shown and in the inset, a central region of the HAADF image. The field of view of the deformation map, the standard deviation in the map and the sampling in the image are indicated. It can be seen that with the exception of the HAADF image with the largest field of view where the atoms are at the limit of being correctly sampled at 4 pixels per lattice spacing, the GPA algorithm is relatively unaffected by the sampling of the atoms with a standard deviation in the range 0.46–0.35% when reconstructed with a spatial resolution of 1 nm. When using HAADF STEM the spatial resolution that is required in the calculated deformation maps is chosen after the experiment during the data processing. Fig. 5 shows ϵ_x maps from the HAADF STEM image of the 157-nm-thick specimen with a field of view of 110 nm that have been obtained using masks in Fourier space to provide a spatial resolutions of (m) 1 nm, (n) 3 nm and (o) 5 nm respectively. Here it can be seen that at lower spatial resolutions the high-frequency noise in the deformation maps is filtered out and the standard deviation in the deformation maps is reduced from 0.46% to 0.18% by reducing the spatial resolution from 1 to 5 nm. Even when a 5 nm spatial resolution is selected, the signal to noise ratio is significantly worse than observed for DFEH.

Additional systematic studies have been performed to assess the effect of dwell time (counts) and the effect of the corrector (by intentionally defocusing the beam). All of these tests have shown that the deformation maps obtained by HAADF STEM are largely insensitive to these experimental parameters. The most important parameter for strain mapping by HAADF STEM is a stable instrument and beam scan. The use of a high-current electron source and a probe corrector to obtain a high intensity electron probe is also important. However, the precision in the strain maps is not high and this technique is best adapted for rapid examination
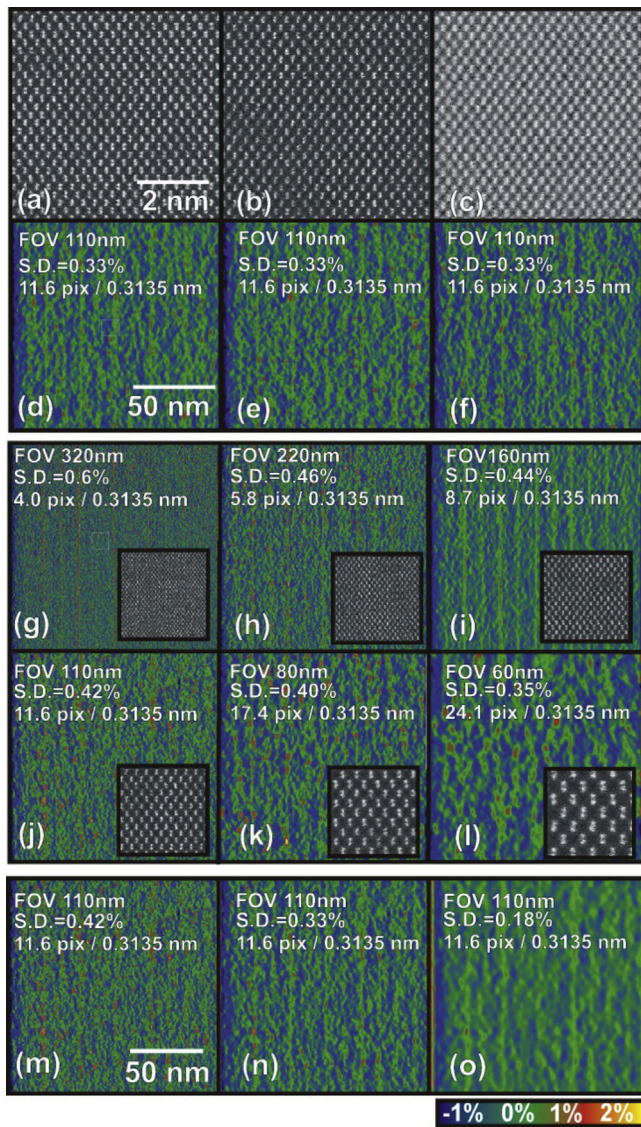
Fig. 5. (a) Shows a 10 nm² detail taken from the centre of a 110 nm² HAADF STEM image of a 157-nm-thick unstrained silicon specimen oriented on the [1 1 0] zone axis and (d) the ϵ_x deformation map calculated with a 3 nm spatial resolution. (b) and (e) as above except for a 184-nm-thick specimen. (c) and (f) for a 286-nm-thick specimen. (g)–(l) show maps of ϵ_x acquired of the 157-nm-thick specimen using increasing magnifications with the central region of the HAADF image shown in the inset to give an idea of the sampling, the total field of view in of the deformation map, the standard deviation and the sampling of the image in nm/pix are indicated. Here a spatial resolution of 1 nm has been selected. Finally ϵ_x maps from the 157-nm-thick specimen that have been calculated using Gaussian masks in Fourier space to provide a spatial resolution of (m) 1 nm, (n) 3 nm and (o) 5 nm.

of the deformation in specimens where a large change in lattice parameter is expected.

Regarding the specimen, deformation mapping by HAADF STEM is very insensitive to preparation. Differences in specimen thickness do not introduce artefacts in the deformation maps. Therefore curtaining effects arising from differential milling under the gate architecture and metal interconnects do not affect the deformation maps, thus back-side milling is not necessary.

2.3. Nanobeam electron diffraction

Nanobeam electron diffraction is a simple technique that can be also be used to provide strain profiles with nm-scale resolution (Naito et al., 2004; Usada et al., 2005). For NBED, a near-parallel
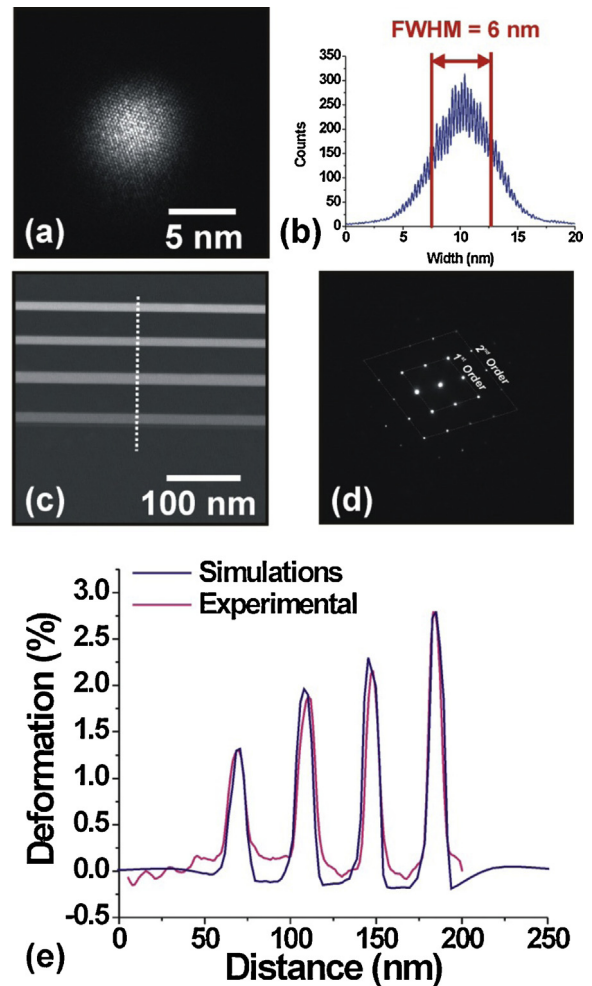

Fig. 6. (a) Image of the probe used for the NBED measurements on Si orientated on the [1 1 0] zone axis. (b) Intensity profile of the parallel probe. (c) The electron beam is scanned across the specimen in STEM mode and a diffraction pattern is acquired at each point. For the experiments performed here, 150 diffraction patterns were acquired over a distance of 200 nm. (d) The strain can be assessed by measuring the shifts in the diffraction spots relative to a diffraction pattern that is usually acquired from the substrate. (e) A ϵ_z profile of the calibration specimen calculated from 150 individual diffraction patterns.

probe is used to form a diffraction pattern. The electron probe is then scanned across the specimen in STEM mode and a diffraction pattern is acquired at each point. Using peak fitting software, large data sets can be quickly analysed and local measurements of the deformation can be generated by comparing the positions of the diffraction spots to a reference. NBED has been demonstrated using microscopes with conventional two condenser lens systems. However, to form a sufficiently parallel electron probe, the beam size is ≃20 nm which is too large for many of the semiconductor devices which are of interest today. If available, a three condenser lens system is preferred in combination with a small (<20 μm) condenser aperture to provide a nm-scale electron probe with a small convergence angle (Béché et al., 2009).

Fig. 6(a) shows an image of the probe used for the measurements incident on the [1 1] zone axis of a silicon sample with a convergence angle of 0.19 mrad. Fig. 6(b) shows that the full width half maximum of the probe is 6.0 nm. That is close to the value predicted by the Rayleigh criterion (6.6 nm), which can be used to estimate the size of the electron probe, $d = 0.5\lambda/\alpha$, where λ is the wavelength of the electron beam and α the convergence angle. Fig. 6(c) shows an image of the calibration specimen formed using the electron probe in NBED mode giving an idea of the spatial
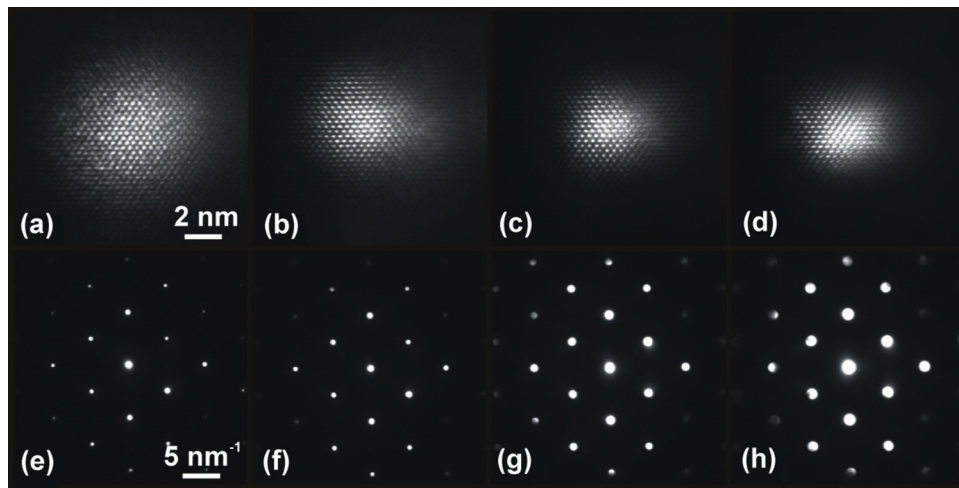
Fig. 7. (a)–(d) effect of apertures to provide electron probes formed using 20, 50, 70 and 100 μm respectively. (e)–(h) corresponding diffraction patterns with a convergence angle of 0.19, 0.76, 1.24 and 1.80 mrads respectively.

resolution of the strain measurement. The electron beam is scanned along a line across the region of interest and (d) the deformation is determined by measuring the relative shifts of the diffraction spots. For the measurements shown here, the displacement of the second order spots is used to calculate the deformation. A ϵ_z profile from the calibration specimen is shown in Fig. 6(e). Here a series of 150 diffraction patterns were recorded to obtain the deformation profile with a pitch of 1.3 nm between each acquisition.

NBED is used extensively in the semiconductor industry (Chen et al., 1999; Okamoto et al., 2008; Toda et al., 2008; Sato et al., 2010; Favia et al., 2010, 2011; Kim et al., 2014a). The problem with NBED is that the spot intensity is not uniform which can lead to an incorrect determination of their positions giving results which are systematically incorrect. Improved spatial resolution can be obtained at the expense of precision by increasing the convergence angle to provide a smaller probe. However, a larger convergent angle will provide wider diffraction spots or discs which are more affected by non-uniformity intensity. Fig. 7 shows the effect of changing the condenser aperture on the beam convergence angle and spot size for a silicon specimen oriented on the [1 1 0] zone axis. Fig. 7(a)–(d) shows the effect of 20, 50, 70 and 100 μm apertures to provide electron probes of 5.8, 3.7, 3.2 and 2.7 nm respectively. The corresponding diffraction patterns are shown in Fig. 7(e)–(h) using 20, 50, 70 and 100 μm apertures to provide beams with a convergence angle of 0.19, 0.76, 1.24 and 1.80 mrads respectively. The specimen has been carefully tilted around the zone axis to provide even intensity in the spots.

The non-uniform contrast present in the diffraction spots is the main problem for NBED and as a consequence this technique is very sensitive to specimen preparation, variations of thickness and bending. Although the sample can be carefully orientated to obtain even intensity in the spots, incorrect results can be obtained in specimens that have small variations across the field of view. Thus the patterns need to be visually inspected to ensure that the spots are evenly illuminated. However, as long as the specimen is perfectly flat there does not seem to be an optimum specimen thickness and NBED can be combined with energy filtering and applied to very thick specimens (Hähnel et al., 2012).

If better spatial resolutions are required, a higher microscope operating voltage can be used. A beam size of 3 nm has been demonstrated by operating an aberration (probe) corrected Titan TEM at 300 kV and using a 50 μm condenser aperture to provide a convergence angle of 0.5 mrads (Béché et al., 2009). If higher spatial resolutions are required without increasing the convergence angle of the beam, an alternative will be to combine higher

brightness guns and longer acquisition times with smaller condenser apertures. NBED has also been used to provide deformation maps (Uesugi et al., 2011; Baumann, 2014) with the main limitations being the movement of the specimen if drift correction is not used and the amount of data that can be recorded in a single series when using commercially available software.

2.4. Precession electron diffraction

As discussed for NBED, the spatial resolution is limited as small electron probes will provide large diffraction discs which are more susceptible to systematic errors that arise from non-even intensity in the spots. A way to remove this problem is to precess the electron beam around each sampling point which provides a more even intensity in the diffracted beams and allows the position of each to be more accurately determined (Vincent and Midgley, 1994). Of course the electron beam can now be made even more convergent in order to provide a smaller probe size (Rouvière et al., 2013). Fig. 8 shows the effect of precessing the beam. A combination of a probe corrector, high-brightness electron gun and 10 μm condenser aperture has been used to provide a small electron probe with a high beam current. In Fig. 8(a) a diffraction pattern is shown which has been acquired using a convergence angle of 2.4 mrads. An image of the probe projected through silicon orientated on the [1 1 0] zone axis is shown in the inset. The problems which were discussed in the NBED section are visible here and the dark features in the diffraction spots would make accurate determination of the position of these spots complicated, even using a sophisticated fitting procedure. Fig. 8(b) and (c) shows the diffraction patterns obtained from the same region of the specimen with the electron beam precessed using 0.25° and 0.50° respectively. Now by integrating the pattern around 2π, the intensities in the diffracted discs are much more even and their positions can be more accurately determined. As such, local measurements of deformation can be obtained by fitting the whole circumference of the discs instead of the maximum intensity in the spots (Müller et al., 2012a). Even though very small angles are used, the precession of the beam does lead to a slight increase in the size of the electron probe as recorded on the specimen. The probe sizes on the specimen shown in Fig. 8(a)–(c) are 1.5, 1.8 and 2.1 nm for precession off, 0.25° and 0.50° respectively.

An array of 50×100 diffraction patterns of the calibration specimen was acquired using a precession angle of 0.25° and was recorded using double binning to provide a 1024^2 camera acquisition with an acquisition time of 0.1 s per pattern. The high-brightness electron gun and monochromator were set to provide
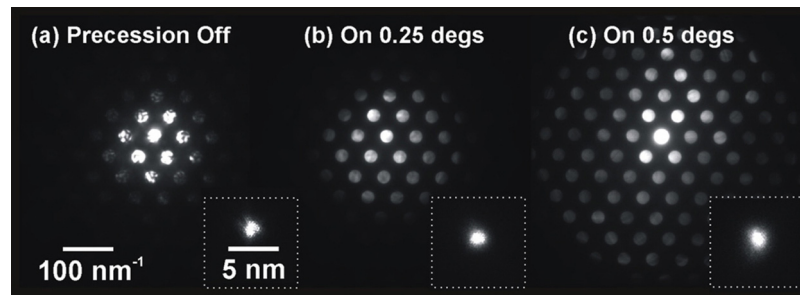
Fig. 8. (a)–(c) The diffraction patterns and size of electron probe (inset) for the N-PED measurements of a silicon sample orientated on the [1 1 0] zone axis with no precession and precession applied at 0.25° and 0.50° respectively.
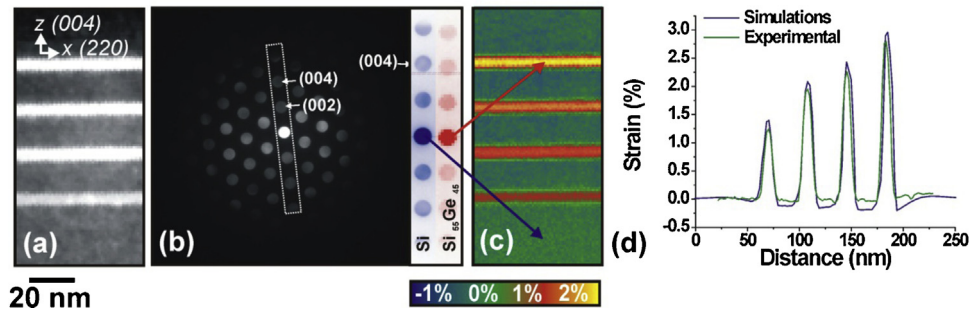

Fig. 9. (a) Pseudo HAADF image of SiGe calibration specimen acquired by using an annular mask in the diffraction patterns. (b) Diffraction pattern acquired of unstrained silicon substrate with the diffracted beams corresponding to the lattice planes in the growth direction indicated. The red beams have been extracted from the indicated area for the unstrained region and the blue beams have been extracted from a diffraction pattern acquired from the $Si_{0.55}Ge_{0.45}$ layer. The shifts of the (0 0 4) diffracted beam can be clearly seen. (c) Deformation map for the [0 0 4] growth direction acquired from 100×50 diffraction patterns scanned with a pitch of 1.5 nm between each recorded image. (d) Experimental and simulated deformation profiles. The experimentally acquired profile has not been averaged and is from a single pattern.

the maximum possible current in the probe. Fig. 9(a) shows a pseudo HAADF image of the SiGe calibration specimen which was obtained by applying an annular mask to the patterns to measure the diffracted intensity at high angles. The four SiGe layers are clearly visible and no specimen drift is observed. Fig. 9(b) shows a diffraction pattern, the spots associated with the lattice planes in the growth direction are indicated. The region of interest has been extracted for illustration and is shown in blue for an unstrained region of the specimen and in red from the $Si_{0.55}Ge_{0.45}$ layer. The shifts in the diffraction discs can clearly be seen. As for the NBED measurements it is the displacement of the seconds order spots that are used to determine the deformation. A ϵ_z map is shown in Fig. 9(c) and a profile extracted from across a single line of pixels of width 1.8 nm in the strain map is shown in (d) and compared to simulations. The N-PED mapping provides an accurate measure of

the strain with greatly improved precision compared to NBED. The approach of using a convergent beam for improving deformation measurement has been exploited previously without precession. Here a high speed camera was used to measure the shifts of CBED patterns in order to provide a precision of between 0.13% and 0.07% for individual acquisition times in the range 1–200 s (Müller et al., 2012b).

For N-PED, the most important experimental parameters that have an influence on the precision in the deformation maps are mainly related to the speed of the data acquisition. The precession speed is 0.1 s for one complete revolution of the beam. This is discretised into 128 individual positions and fixes the lower limit of the acquisition time for each diffraction pattern. Fig. 10(a) shows 15×15 pixel ϵ_x deformation maps for a 157-nm-thick unstrained silicon specimen orientated on the [110] zone axis. The step size
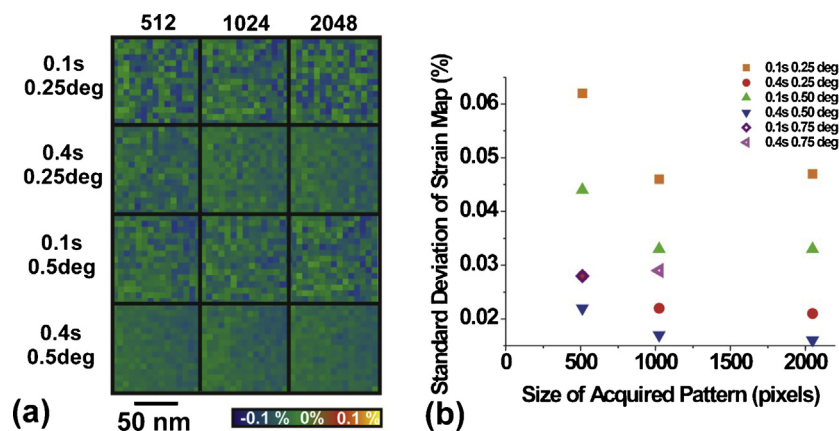

Fig. 10. (a) Deformation maps measured using 15×15 diffraction patterns with a step of 5 nm orientated on the [1 1 0] zone axis for the in plane direction using different precession angles and camera pixel sizes obtained by binning. The standard deviation in the maps as a function of the camera binning is shown in (b).
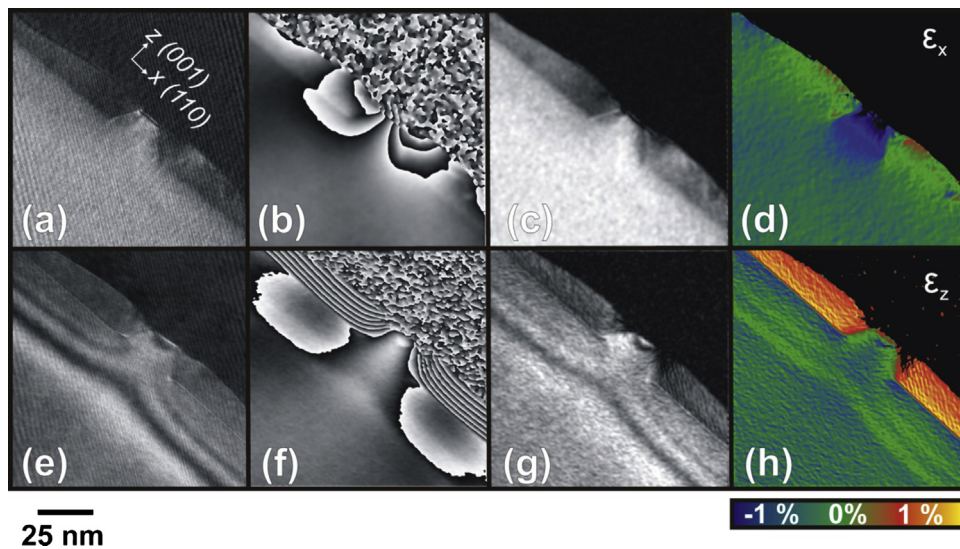
Fig. 11. (a) Dark hologram for the (2 2 0) diffracted beam, (b) corresponding phase image, (c) amplitude image and (d) deformation map, ϵ_x. (e) Dark hologram for the (0 0 4) diffracted beam, (f) corresponding phase image, (g) amplitude image and (h) deformation map, ϵ_z.

between each diffraction pattern is 5 nm to provide a sampled area of ~75 nm. As the precision is given by the accuracy of the measurement of the diffraction spots, acquisition parameters such as the pixel size of the recorded images, the acquisition time and the precession angle have been varied. Fig. 10(b) shows the measured standard deviation of the different deformation maps. The dead time needed to read the data out of the CCD camera is relatively large compared to the precession frequency. The total recording time, including read-out for a single 1024^2 image on the FEI Titan Ultimate at CEA equipped with a Gatan Orius 830 camera is 1.4 s for a recording time of 0.4 s. This can be compared to 1.1 s when a recording time of 0.1 s is used. Fig. 10(b) shows that by using a nominal acquisition time of 0.4 s instead of 0.1 s, the precision in the measurement is more than doubled, even though the total recording time of each image is only increased by less than 30%. It can also be seen that for a 2048^2 acquisition, an acquisition time of 0.4 s and a precession angle of 0.5°, a standard deviation of 0.015% is observed in the deformation map. Even when a 512^2 acquisition is used with a 0.4 s acquisition time and 0.25° precession angle is used, a standard deviation of better than 0.03% is obtained. These values compare well to the best sensitivities that can be obtained using DFEH. For the settings used here, the precession angle does make a difference to the precision of the results as the second order diffraction discs are used for the measurements. This is not always the case and a theoretical study discussing the optimum settings that can be used to provide deformation maps by both NBED and N-PED is available (Mahr et al., 2015).

3. Strain mapping applied to different types of specimens

3.1. Deformation in a conventional bulk-type semiconductor device.

The semiconductor device chosen for this comparative study comprised SiO_2/Si_3N_4 dummy gates with a gate length of 35 nm and recessed SiGe sources and drains with a Ge concentration of 35% (Cooper et al., 2010a,b, 2011a,b). The SiGe device specimen was realised by depositing a 50-nm-thick Si_3N_4 layer onto a 10 nm SiO_2 layer on a Si(0 0 1) wafer. The films were then patterned to form 0.1 μm lines each separated by 0.4 μm of Si. The silicon was then etched using gaseous HCl to leave {1 1 1} recess sidewalls under the gates with channel lengths of 35 nm. These recesses were then filled with undoped SiGe using RPCVD. Uniaxial deformation in the

silicon channel arising from both the recessed SiGe sources and drains and an effect from the Si_3N_4 film is expected (Denneulin et al., 2012).

Fig. 11(a) shows a dark hologram acquired of a 130-nm-thick specimen using the (2 2 0) diffracted beam. Here a fringe spacing of 1.7 nm and field of view of 290 nm has been chosen. An acquisition time of 64 s was used to increase the number of recorded electron counts. In order to obtain a two beam condition, the specimen has been rotated around the x-axis by approximately 2° which leads a spreading of information of 4.5 nm in projection which can be observed in the dark hologram and amplitude image. The objective lens was excited to 25% to allow the diffracted beams to be positioned down the optical axis in dark field mode (Wang et al., 2004). Fig. 11(b) and (c) shows the corresponding phase and amplitude images respectively which have been reconstructed using a mask to provide a nominal spatial resolution of 5.5 nm. Fig. 11(d) shows the ϵ_x deformation map demonstrating that as expected the SiGe recessed source and drain regions are in epitaxy with the silicon substrate and that the channel region has been compressed. Fig. 11(e) shows a dark hologram acquired using a (0 0 4) diffraction spot and the same experimental settings as described in (a). Fig. 11(f), (g) and (h) shows the reconstructed phase, amplitude and ϵ_z deformation map. From the ϵ_z map it can be seen that the lattice parameter in the SiGe regions has been expanded in the z-direction which is consistent with the ϵ_x deformation map.

Fig. 12 shows the results obtained using HAADF STEM. Given the small dimensions of the device, it was experimentally straightforward to acquire a 4096^2 pixel image with the atoms correctly sampled. In this case 9.2 pixels were used to sample each atomic spacing in the x-direction observed on the [1 1 0] zone axis whilst still maintaining a large area of unstrained reference in the 140^2 nm field of view. Fig. 12(a) shows the acquired HAADF image and (b) the Fourier transform indicating the two different (1 1 1) spots that were selected using a Gaussian mask to provide a spatial resolution of 3 nm. The corresponding phase images are shown in Fig. 12(c) and (d) as well as the deformation maps for (e) ϵ_x, (f) ϵ_z. In this case, the shear strain (g) ϵ_{xz} and (h) rotation maps are also shown as it is straightforward to obtain this information from the two different diffracted beams. The experiment is performed with the specimen aligned on the zone axis and no complicated alignments are required. It can be seen that the ϵ_z map is affected by scan distortions and that these dominate the deformation measurement.
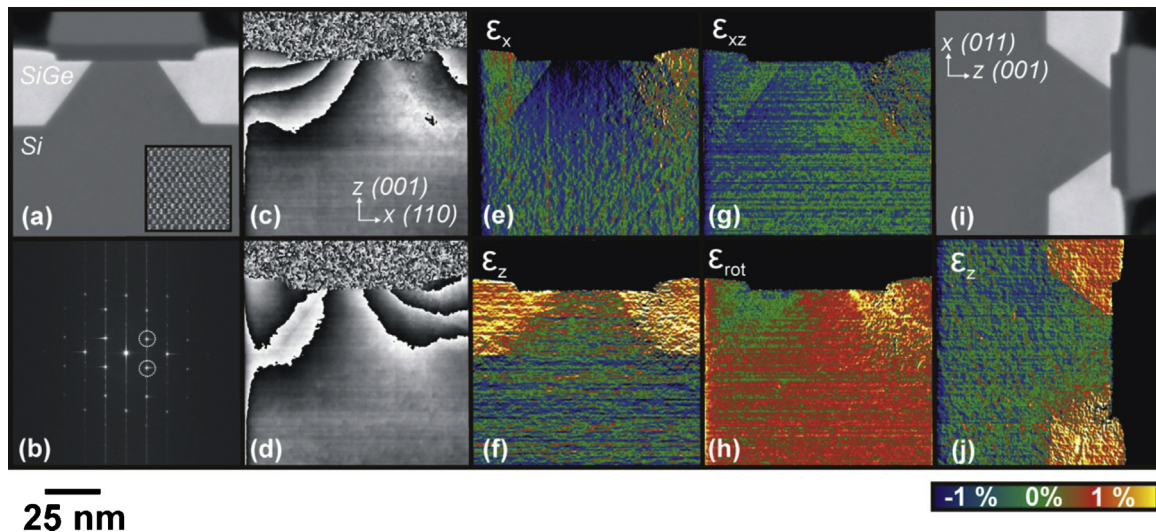
Fig. 12. (a) HAADF STEM image of SiGe device with detail of image shown in inset and (b) shows corresponding FFT. (c) and (d) Corresponding phase images for two (1 1 1) spots extracted from the FFT from which deformation maps for the (e) ϵ_x, (f) ϵ_z, (g) ϵ_{xz} and (h) rotation. (i) HAADF STEM image of SiGe device with scan direction rotated by 90° and (j) corresponding deformation map for ϵ_z.

Fig. 12(i) shows that by rotating the scan direction by 90° (j) a ϵ_z deformation map can be obtained without these distortions.

Fig. 13(a) and (b) shows deformation maps for the ϵ_x and ϵ_z directions obtained using a fast precession diffraction acquisition. Here 50×25 diffraction patterns were acquired using an acquisition time of 0.1 s and a camera binning of 8 which gives 256 pixel images. These parameters allowed the data series to be acquired in less than 10 min and data processing took less than 1 min. The pitch of the acquisitions is 3.5 nm using an electron probe of 1.8 nm diameter. These deformation maps can be compared to Fig. 13(c) and (d) which show equivalent deformation maps using 100×50 diffraction patterns each acquired for 0.1 s using a camera binning of 2 to provide 1024 pixel images. Here the pitch of the acquisition is 1.75 nm with an electron probe of 1.8 nm. The experiment took 90 min with no significant specimen drift observed during the acquisition. There is an improvement in both the spatial resolution and precision, and details which are not observable in the fast acquisition can be seen in the detailed acquisition. For completeness, the (e) ϵ_{xz} and (f) rotation maps are also shown.

Fig. 14 shows ϵ_x deformation profiles acquired from under the gate towards the substrate for all of the techniques that have been discussed here. These profiles have been compared to finite element simulations that account for the effect of the 50-nm-thick silicon nitride film as well as the SiGe recessed source and drains (Cooper et al., 2015). Each profile has been averaged across different widths in order to provide an optimum signal to noise ratio. The DFEH profile has been averaged across 3.6 nm, the HAADF STEM across 10 nm, the NBED is from a single profile acquired from a 6 nm probe and the N-PED is a single profile acquired from a 1.8-nm-sized probe. All of the experimental results are consistent with each other and also consistent with simulations which confirms that all of these techniques are suitable for the measurement of deformation in simple semiconductor devices where large values of deformation are expected. For all of the different maps, multiple profiles are shown which were acquired on different devices (from the same TEM specimen during the same microscope session) in order to show the reproducibility of the techniques.

3.2. Nitride stressors

To improve the mobility in pMOS devices SiGe is used to provide compressive strain. For nMOS devices tensile strain is required.
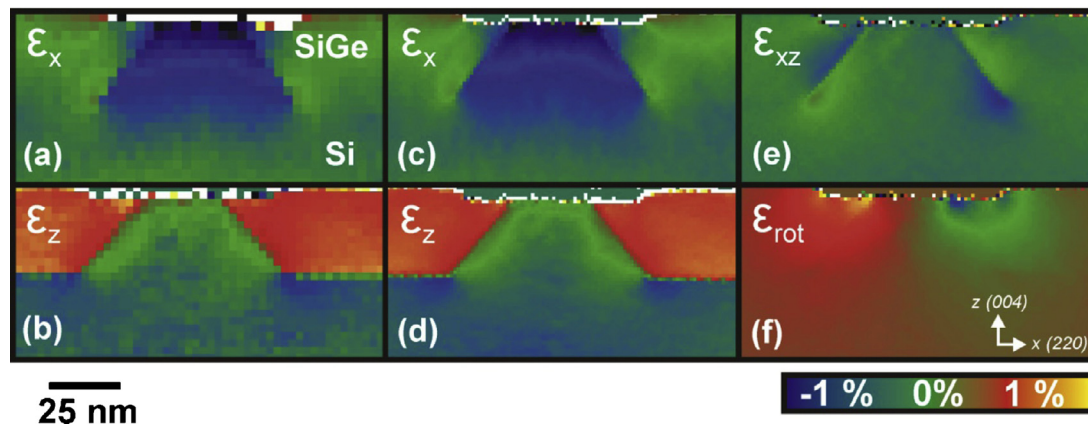

Fig. 13. Deformation maps for the (a) ϵ_x and (b) ϵ_z directions acquired using 50×25 diffraction patterns, camera binning eight and a nominal acquisition time of 0.1 s per image. The total time for the data acquisition is less than 10 min with data processing of less than 1 min. Deformation maps for the (c) ϵ_x and (d) ϵ_z directions using 100×50 diffraction patterns, camera binning 2 and a nominal acquisition time of 0.4 s per image. The total time for the data acquisition here is 90 min with 1 h of processing time. For completeness, deformation maps for (e) ϵ_{xz} and the (f) rotation acquired are also shown.
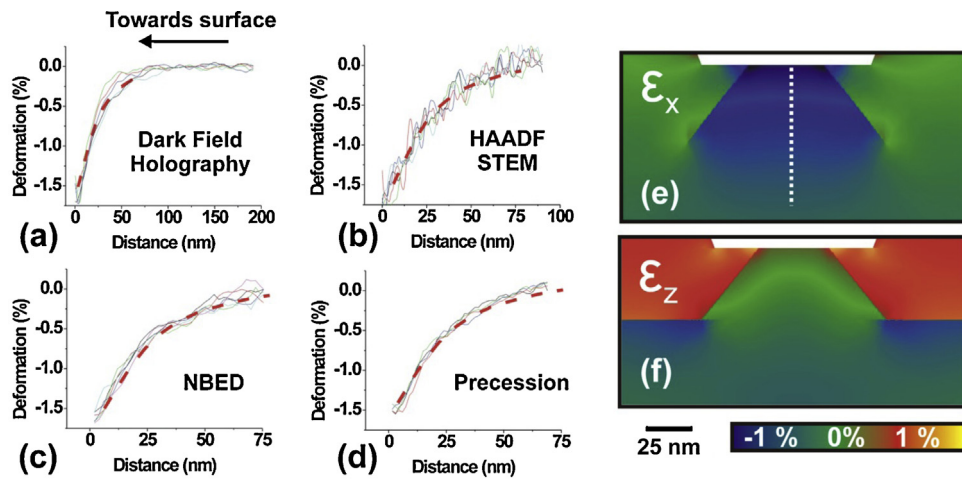
Fig. 14. Deformation profiles for the ϵ_x direction acquired using (a) DFEH, (b) HAADF STEM, (c) NBED and (d) N-PED. For completeness, finite element simulations for the (e) ϵ_x and (f) ϵ_y directions are also shown. For comparison, the simulated profile is superimposed onto the experimental data using the dashed line.

One strategy is to use silicon nitride films (known as a contact etch stop layer or CESL) which introduces a relatively low value of tensile deformation which from the point of view of electron mobility provides a significant improvement (Eneman et al., 2007). As the deformation that is introduced in the devices by the nitride films is dependent on both deposition parameters and subsequent wafer processing, it is important to have an independent measure of the effectiveness of the films as stressors. The measurement of these low values of strain is difficult. Thus these specimens make an ideal test for the different strain mapping techniques (Cooper et al., 2011a).

Specimens were prepared using backside milling from a 28 nm high-k metal gate nMOS device. The backside milling is required to avoid curtaining from the metal layers in the device which in this case is the high-k metal gate (Overwijk et al., 1993). The specimens were left relatively thick (180 nm) to ensure that the

nitride film would not become detached from the silicon substrate during preparation. Fig. 15(a) shows a bright field STEM image of the device array that was examined. This array is a test region with 9 devices with a pitch of 120 nm which is designed on a working chip to allow characterisation on the devices without the complications of the metal contact layers and salicidation. To improve the mobility of the pMOS devices that are present on the same wafer, the devices are grown with a 45° rotation compared to older generation semiconductor devices so that the specimen is now oriented on the [0 0 1] zone axis.

Fig. 15(b) shows a ϵ_x deformation map obtained by N-PED, here the map was calculated using 50 × 25 diffraction patterns recorded using a 1024^2 acquisition. As the specimen was observed down the [0 0 1] zone axis, it was necessary to use a higher precession angle than normal of 1° to provide an even intensity across the second order diffracted beams that are used to calculate of the deformation.
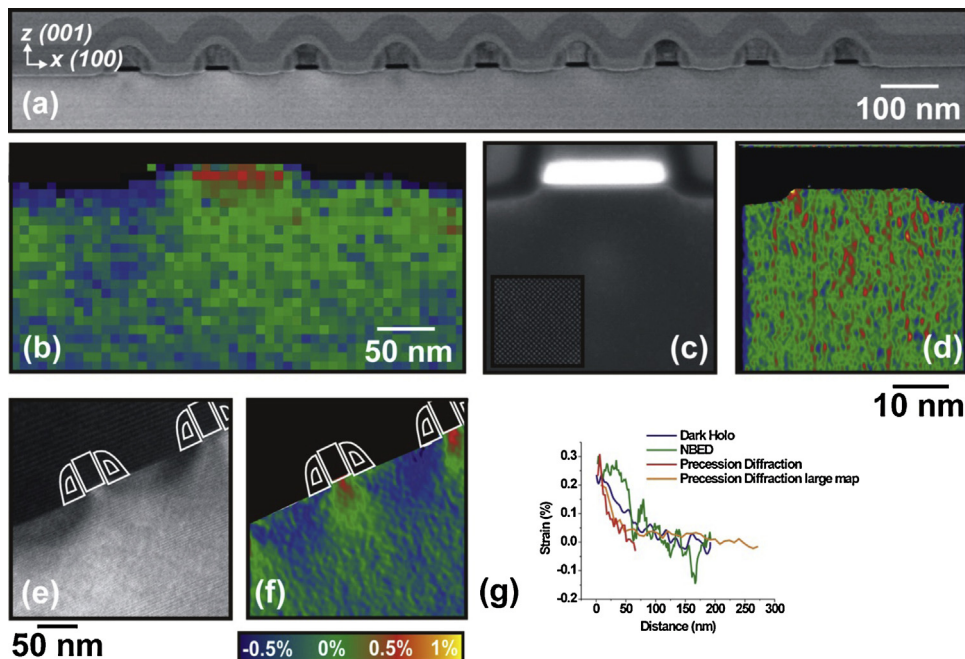

Fig. 15. (a) BF STEM image of the sample examined. (b) Deformation map for ϵ_x acquired using N-PED. (c) HAADF STEM image of a device and (d) corresponding deformation map for ϵ_x. (e) Dark hologram using the (1 0 0) diffracted beam and (f) corresponding x deformation map. (g) ϵ_x deformation profiles acquired by DFEH, N-PED, NBED and HAADF STEM. An additional N-PED profile taken from a data set with a larger field of view is also shown. To be able to properly display the results, the contrast scale is different to the other data sets shown in this manuscript.

Using this larger precession angle, a spot size of 2.5 nm is measured on the specimen and a spatial resolution in the strain map is now 5.0 nm due to angular path of the beam through the specimen. Here a deformation of 0.3% is measured directly under the gate which rapidly decays to zero at 50 nm depth into the substrate.

Fig. 15(c) shows a HAADF STEM image of the device, with a detail from the image in the inset in order to show the sampling of the atoms and (d) shows the ϵ_x deformation map obtained from this image. Although each atomic spacing has been sampled by 14 pixels and the deformation map has been calculated using a small mask to provide a spatial resolution of 5 nm, it is dominated by noise and no deformation under the gate is observed. In addition, for this magnification it is difficult to be sure that the reference that is used in the field of view is unstrained. To include an unstrained region a lower magnification can be used which would have the effect of introducing more noise due to less sampling of the atoms. An alternative approach would be to acquire a reference STEM image from the substrate which can also be used as a reference simply by cutting and pasting part of this into the STEM image of the device. If this approach is used, it is preferable to use beam shift as moving the specimen can also have the unintended effect of changing the specimen height.

Fig. 15(e) shows a dark hologram using a (1 0 0) diffracted beam and (f) the corresponding ϵ_x deformation map. To obtain the appropriate two-beam condition, the device has been rotated to 1.5° around the z-axis which leads to a spreading of information of 4 nm in the z direction. The spatial resolution in the map determined by the 1.7 nm fringe spacing is 5.0 nm. The results show that DFEH has the precision to measure the deformation in these types of devices. However, care must be taken as the deformation map obtained by DFEH is also affected by the doping in the device. The high dopant concentrations that are used in today's semiconductor devices will lead to sharp steps in electrical potential will also change the phase of the electrons. The dopants however do not significantly effect ϵ_x in the region of interest which is directly under the gate as this region does not contain the sharp variations electrical potential which could be misinterpreted as deformation.

For the NBED experiments, the experimental procedure as described previously was used, however, it was extremely difficult to obtain strain profiles that were consistent with those obtained from the other techniques due to the non-uniformity in the spots. Experimentally it was difficult to acquire a data series with a good enough signal to noise ratio and multiple attempts were required in order to obtain a "good" dataset.

Fig. 15(g) shows deformation profiles acquired from all of the different techniques compared, in all cases a tensile strain in the range 0.2–0.3% has been recovered. For the N-PED, two profiles are shown, one extracted from Fig. 15(b) and another from a different data series which measures the deformation deep in the substrate using a larger step size between each pattern. The HAADF STEM and the NBED results do not provide adequate precision for deformation mapping for these types of specimen. DFEH is well adapted for the study of nitride films as it is quick and straightforward to perform this experiment using the silicon substrate as a reference. The disadvantages with DFEH is that the phase is very sensitive to thickness variations in the specimen and back-side milling is required due to the presence of the high-k metal gate. This advanced specimen preparation can take a skilled operator 3–4 h to complete instead of 1–2 h for standard FIB preparation. In addition, there can be complications from the phase changes arising from active dopants in the specimen. N-PED has the sensitivity for the measurement of deformation in these types of specimens. Although N-PED can take longer to perform in the TEM for large and detailed maps, it is not sensitive to thickness changes in the specimen and as a consequence, the specimen can be prepared using standard milling techniques.

3.3. Silicon on insulator technology

Silicon-on-insulator (SOI) technology uses transistors which are grown on a thin silicon layer on an oxide layer known as the BOx (Bruel, 1995). Due to this insulator layer there is a reduced leakage path when the devices are in the off state and as such are promising candidates to be used for future device technologies (Weber et al., 2014). These types of devices are also of interest in terms of benchmarking different strain mapping techniques for two reasons. There is a misorientation between the silicon substrate and the top silicon layer known as the miscut, and these devices are extremely small with the top silicon layer being as small as 8 nm in state of the art devices (Cooper et al., 2012a,b). The complexity of these devices, as well as the potential to engineer strain using a range of different methods makes deformation mapping extremely important. But the measurement of deformation in SOI device is known to be complicated (Hähnel et al., 2011) and as such, systematic studies are often performed on thin films instead of fully processed devices (Boureau et al., 2015).

For this study, two different fully processed and electrically tested SOI pMOS device were prepared from the same wafer by back-side FIB milling. The first device had a gate length of 25 nm and was examined by DFEH and NBED. However, this specimen was damaged and an adjacent device on the wafer with a gate length of 50 nm was prepared for the HAADF STEM and N-PED experiments. Fig. 16(a) shows a STEM image of the 25-nm-gate device that was used in these tests. The device was grown on a strained silicon layer which has the same lattice parameter as a $Si_{0.8}Ge_{0.2}$ film. On top of this layer a 20-nm-thick $Si_{0.6}Ge_{0.4}$ layer has been grown and then etched to leave a 25-nm-wide SiGe channel with a silicon source and drain either side. The goal is for the $Si_{0.6}Ge_{0.4}$ channel to be compressively strained by the tensely strained silicon layer beneath it. This device is actually large compared to real state-of-the-art SOI devices, however this example was chosen in order to be able to apply all of the different deformation mapping techniques on it.

Fig. 16(b) and (c) shows a hologram acquired using DFEH in Lorentz mode using the (2 2 0) diffracted beam and the associated ϵ_x deformation map. Experimentally this is an extremely difficult experiment to perform as the substrate and the region of interest are mis-aligned by 1.0 mrads. The complication arises that it is not possible to have the region of interest and reference exactly in a two-beam condition at the same time. In order to acquire a dark field electron hologram of this real device, the 150-nm-thick specimen was tilted to 2° from the x-axis which leads to a spatial resolution imposed by the projection of the specimen of 5 nm. The fringe spacing in the hologram was set relatively large at 2.5 nm as the experiment was difficult and thus the more pixels were required to record each fringe to improve the measured contrast. However, this leads to a spatial resolution of only 7.5 nm in the deformation map. Experimentally it was not possible to achieve a ϵ_z deformation map using the (0 0 4) diffracted beam due to combinations of the miscut and small device dimensions regarding the required specimen tilt.

Fig. 16(d) and (e) shows a hologram acquired using objective lens mode using the (2 2 0) diffracted beam and the associated ϵ_x deformation map. In conventional objective lens mode, the field of view is only a few tens of nanometers which is unsuitable for DFEH of these types of semiconductor devices, however, by operating the microscope in free lens control, the field of view can be expanded and holograms with a very fine fringe spacing can be achieved (Sickmann et al., 2011). Here a fringe spacing of 0.38 nm has been obtained with a contrast of 10% in the region of interest. Although the deformation map was reconstructed to have a spatial resolution of 1 nm, it is still the tilt of the specimen in the two-beam condition that limits the spatial resolution in the deformation map
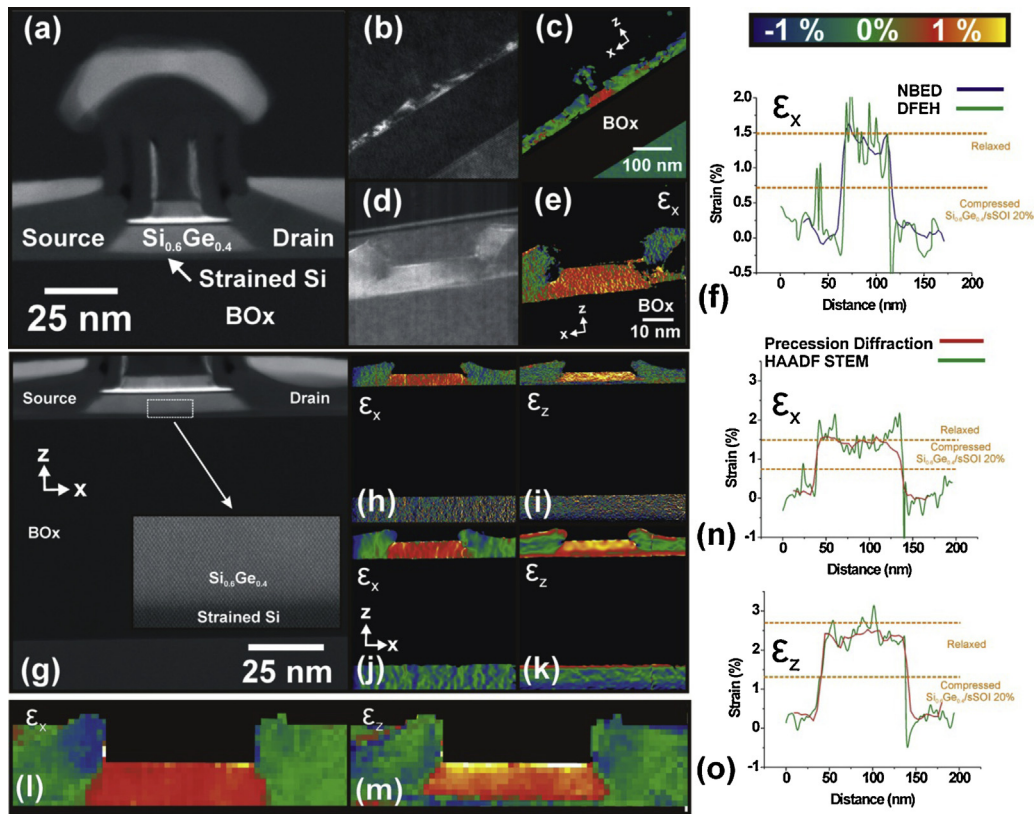
Fig. 16. (a) HAADF STEM image of a p-MOS silicon on insulator type device grown on a 145-nm-thick Box and a gate length of 25 nm. (b) Dark hologram acquired using conventional Lorentz mode with the (2 2 0) diffracted beam selected and (c) deformation map for ϵ_x. (d) Dark hologram acquired using a fringe spacing of 0.38 nm in free lens objective mode and the (2 2 0) diffracted beam (e) corresponding deformation map for ϵ_x. (f) ϵ_x deformation profiles for the DFEH in conventional Lorentz mode and NBED that have been extracted from across the channel. (g) HAADF STEM image of a device with a gate length of 50 nm. (h) and (i) Deformation maps for the ϵ_x and ϵ_z directions obtained by HAADF STEM using a mask to obtain a spatial resolution of 1 nm. (j) and (k) Deformation maps for the ϵ_x and ϵ_z directions obtained by HAADF STEM using a mask to obtain a spatial resolution of 5 nm. (l) and (m) Deformation maps for ϵ_x and ϵ_z acquired using N-PED. (n) and (o) Deformation profiles taken from across the gate in the region indicated in (f) for ϵ_x and ϵ_z acquired by HAADF STEM and N-PED.

and this can be seen in Fig. 16(d) and (e) at the top and bottom of the SiGe channel region.

The NBED was performed using a standard convergence angle of 0.19 mrads and a 6 nm beam diameter. Data series of 100 patterns were acquired using an acquisition 1024^2 pixels and a reference acquired from the unstrained silicon substrate. Fig. 16(f) shows ϵ_x deformation profiles that have been extracted from the centre of the device in the indicated region in (a) for the Lorentz DFEH and NBED. As the $Si_{0.6}Ge_{0.4}$ channel was grown on strained silicon with a lattice parameter of $Si_{0.8}Ge_{0.2}$, then if it is in epitaxy and not relaxed then Vegard's law suggests that ϵ_x should be 0.7% relative to the unstrained silicon reference. Both the NBED and DFEH measure a deformation in the $Si_{0.6}Ge_{0.4}$ channel of 1.4%. Thus the strained silicon layer has not succeeded in compressing channel as it is fully relaxed. The DFEH deformation profile is much noisier than would be expected for a perfect bulk-like specimen, however, it is possible to see that the channel is relaxed. In addition, dislocations can be observed in the source and the drain region of the device in both the DFEH map and in profiles where very sharp peaks in the deformation are observed. The NBED was appropriate to measure the deformation in these devices as the 20-nm-thick $Si_{0.6}Ge_{0.4}$ channel is larger than the probe. The latest generation devices are often much smaller than this and better spatial resolutions are required. Fig. 16(g) shows a HAADF STEM image of the 50-nm gate device. Fig. 16(h) and (i) shows deformation maps obtained from the HAADF STEM image in (g) for the ϵ_x and ϵ_z directions that have been calculated with a mask in Fourier space to provide a spatial resolution of 1 nm. Here the 2-nm-thick strained silicon layer in the ϵ_z map is resolved. The signal-to-noise ratio in the region of interest

is better than in the substrate due to the miscut of the wafer. For the experiment, the region of interest is on the zone axis and the substrate is slightly mis-orientated. Fig. 16(j) and (k) shows ϵ_x and ϵ_z deformation maps that have been calculated with a spatial resolution of 5 nm. The precision of the measurement has been improved, however, the strained silicon layer is not clearly resolved and thus the map does not show the true deformation distribution in this device. Fig. 16(l) and (m) shows deformation maps of the device for the ϵ_x and ϵ_z directions acquired using N-PED. The maps have been calculated using an acquisition of 50×25 diffraction patterns which were recorded using a 1024^2 pixels and a precession angle of $0.25°$ leading to a spatial resolution of 2 nm. Here the strained silicon later has been resolved. Fig. 16(n) and (o) shows deformation profiles that have been extracted from the HAADF STEM and N-PED maps for the ϵ_x and ϵ_z directions respectively. Again, the results are consistent with one another and show that even for a 50-nm-gate the $Si_{0.6}Ge_{0.4}$ has fully relaxed and that this relaxation in the critical ϵ_x direction is consistent across the whole channel.

Both HAADF STEM and N-PED have shown that they are adapted for measuring the strain in SOI-type devices. Although the device examined here is not particularly small from the point of view of state-of-the-art semiconductor devices, it has shown that DFEH and NBED can struggle from the point of view of spatial resolution due to the tilting required for holography and the beam size for NBED. DFEH can also give inaccurate results in the case of a high miscut and NBED inaccurate results from dynamical diffraction which is more difficult to eliminate in real devices. The poor precision in HAADF STEM is a problem, however this technique has been used for performing systematic studies for the latest generations
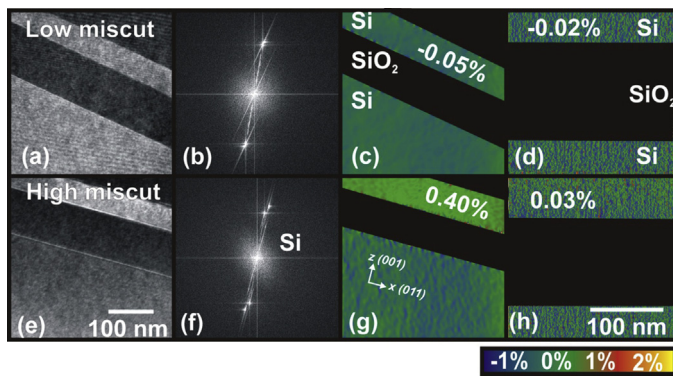
Fig. 17. (a) Dark hologram acquired using the (2 2 0) diffracted beam of a unstrained silicon on SOI with low miscut, (b) Fourier transform of the hologram and (c) ϵ_x deformation map. (d) Shows the ϵ_x deformation map acquired by HAADF STEM. (e) Dark hologram acquired using the (2 2 0) diffracted beam of a unstrained silicon on SOI with a high miscut. (f) Fourier transform of the hologram showing a double spot pattern in the sideband and (g) ϵ_x deformation map. (h) Shows the ϵ_x deformation map acquired by HAADF STEM. The measured deformation in the unstrained silicon layer is shown in the maps.

of devices with nanometer scale dimensions (Morvan et al., 2013). N-PED has been developed more recently, but is already being used routinely to provide useful information with the both required spatial resolution and precision about deformation in these types of devices. From the point of view of accuracy of the measurements, simulations have shown that for the very small dimensions that are used in these devices, a large degree of relaxation in the thin TEM specimens is not expected. However, simulations should always be performed for all different types of devices to assess the effect of thin foil relaxation.

To compliment this study, the effect of the miscut on the measured deformation has been investigated. Two thick unstrained silicon films grown on a 145-nm-thick BOx with known mis-orientations relative to the substrate were investigated by DFEH, N-PED and HAADF STEM. The mis-orientation was independently measured by X-ray diffraction. The first wafer has a relatively low miscut of 1.4 mrads around the z-axis which corresponds to a typical value of miscut for a SOI type wafer. Fig. 17(a) shows a dark hologram acquired using the (2 2 0) diffracted beam and (b) a Fourier transform of the hologram. Fig. 17(c) and (d) shows ϵ_x deformation maps acquired using DFEH and HAADF STEM respectively. The HAADF STEM deformation measurements were calculated to provide a spatial resolution of 5 nm to improve the precision. No deformation is expected in the top layer however, a deformation of $0.05 \pm 0.02\%$ has been measured by DFEH and $-0.02 \pm 0.19\%$ for the HAADF STEM. An additional specimen with a very large miscut was also examined with a rotation of -7.1 mrads around the z-axis. Fig. 17(e) and (f) shows a dark hologram acquired using the (2 2 0) diffracted beams and a Fourier transform of the hologram respectively. Here it can be seen that there are two spots in the sideband which is unexpected. From the ϵ_x deformation maps acquired by DFEH and HAADF STEM that are shown in Fig. 17(g) and (h), values of deformation of $0.40 \pm 0.02\%$ and $0.03 \pm 0.19\%$ are measured. For the wafer with the large miscut, the deformation measured by DFEH is significant and cannot be explained simply from the super-position of the **g**-vectors between the region of interest and the substrate viewed at the miscut angle. A modification of the deformation would also be expected from HAADF STEM as the lattice spacing would be reduced when viewed at an angle relative to the substrate. For the largest miscut observed here this would lead to a modification of the deformation of 0.000025% which is not significant compared to experimental error. Indeed the HAADF STEM measurements of the same wafer show that the top silicon layer is not strained to within experimental error. N-PED measurements

(only profiles and not maps were acquired and these are not shown here) on these specimens also showed that the top layers of the specimens were unstrained. Thus care must be taken when using DFEH to measure the deformation in specimens where the reference and the region of interest are not in alignment as the results can be inaccurate. However, for the majority of SOI-type devices, the miscut tends to be in the region of 1 mrad, and as such this problem is not serious.

3.4. AlGaN superlattice

Silicon devices are grown on high quality wafers and the epitaxial growth of materials such as SiGe are very well controlled. For other types of semiconductors such as III/V and II/VI superlattices there can be many problems from the imperfections of the layers (Jones et al., 2013). To investigate the strengths and weaknesses of the different deformation mapping techniques, a superlattice comprising 6 layers of GaN(16 nm)/AlN(13 nm) grown on a 60 nm thick AlN layer on a $(1-1 0 0)$ SiC substrate was examined. For this sample, large values of deformation are expected, but also many defects will be present. A specimen was prepared using FIB milling to provide a 140-nm-thick lamella which was orientated on the $[1 1 -2 0]$ zone axis for the deformation measurements in the TEM.

Fig. 18(a) shows a dark field electron hologram with the (0 0 0 2) diffracted beam selected in order to measure the deformation in the growth direction. Fig. 18(b) shows the reconstructed amplitude image. In a perfect specimen, the contrast in the different layers should be even, thus this image indicates that there are many defects and dislocations present. Fig. 18(c) shows the ϵ_z deformation map acquired by holography. As suggested by the amplitude image, the map is full of information about the defects and dislocations. In this case, the deformation in the region of interest is relative to the unstrained and crystallographically perfect SiC, however, if the reference area in the sample also contained defects then the measured phases would be difficult to interpret. Fig. 18(d) shows a 20×85 pixel ϵ_z deformation map obtained by N-PED using a probe size of 2 nm, a precession angle of 0.25° and a pitch of 4 nm. Here the 60-nm-thick AlN layer has been used as the reference. A precision of $\pm 0.10\%$ has been measured in this measurement by taking the standard deviation in the AlN region. This is much larger than usually observed for N-PED measurements and this is not due to experimental error but from variations in deformation in this layer. NBED experiments were also performed using a probe size of 6 nm and a convergence angle of 0.19 mrads and a 200 pattern series to provide a measure of the deformation in the growth direction. The measurement by NBED was straightforward to perform due to the high values of deformation present and the relatively thick layers compared to the size of the beam.

Fig. 18(e) shows a 2k × 8k HAADF STEM image of the specimen. Here each atomic spacing measuring 0.267 nm in the z-direction was sampled using 5.6 pixels. Fig. 18(f) shows the ϵ_z deformation map calculated to provide with a spatial resolution of 2 nm and a precision of $\pm 0.25\%$. HAADF STEM is suitable for measurement of the large values of deformations that are measured here, corresponding to GaN having a lattice parameter which is 3.5% larger than AlN or 4.0% larger than the SiC. However, the precision would not suitable for measurements such as an assessment of the composition in the layers from the deformation. Profiles showing the deformation measured using all the different techniques are shown in Fig. 18(g) and (h) and are compared to finite element simulations that account for relaxation in the 140-nm-thick specimen. All of the experimental results are in reasonable agreement with the finite element simulations, however, it is not useful to compare the values of strain measured by the different techniques due to the local variation of deformation across the sample given that the experiments were not performed on the same region.
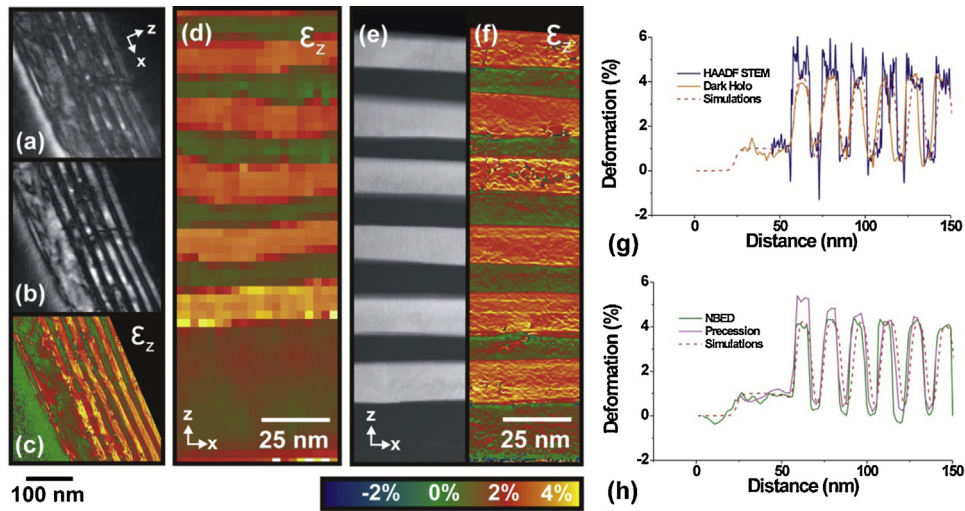
Fig. 18. (a) Dark Hologram from the AlN/GaN superlattice acquired using a (0 0 0 2) beam. (b) Corresponding amplitude image and (c) ϵ_z deformation map. (d) ϵ_z deformation map acquired by N-PED. (e) 2k by 8k HAADF STEM image and (f) corresponding ϵ_z deformation map. (g) ϵ_z deformation profiles acquired by HAADF STEM and DFEH compared to finite element simulations. (h) ϵ_z deformation profiles acquired by N-PED and NBED compared to finite element simulations.

NBED and N-PED exploit only the positions of the diffracted beams and are thus less complicated to interpret than techniques that measure the phase of the electrons. As such the ϵ_z deformation profiles acquired by DFEH seem relatively noisy. This is because phase of the electrons are extremely sensitive to defects and dislocations (Cherns and Jiao, 2001) and as such it is difficult to interpret all of the information in the deformation map. High densities of dislocations can also complicate the accurate measurement of the positions of the atoms for images acquired by HAADF STEM. For this superlattice specimen, the different techniques are complimentary. N-PED will measure accurately the average deformation in the device, the DFEH will reveal the positions and can provide information about the strain fields around individual dislocations and the HAADF STEM will provide valuable information at an atomic scale.

4. Discussion and outlook

4.1. Summary of techniques as applied to the samples

The four different deformation mapping techniques have been applied to a range of different specimens which each have different problems associated with them. Characterisation techniques are often benchmarked only using simple calibration specimens and blanket films which do not reveal all of the problems that are encountered when performing materials science on real devices. Indeed for the simple calibration specimen which is perfect in terms of the epitaxy, there are few problems observed for any of the techniques for performing the experiment. DFEH and N-PED provide the best precision, HAADF STEM provides the best spatial resolution with the worst precision. All of the different techniques measure the same value of deformation in the SiGe layers which agree with finite element simulations. To give a comparative feel of the spatial resolution and precision for the different techniques, Fig. 19 shows a montage of (a) a HAADF STEM image and ϵ_z maps acquired using (b) HAADF STEM, (c) DFEH, (d) N-PED and (e) finite element simulations for the calibration specimen.

The simple 35-nm-gate SiGe device adds challenges, despite only being a test device and having almost perfect crystal quality without the presence of salicidation and metal contacts. Already it is an advantage to perform the experiment with the device oriented on the zone axis as for these types of devices the interesting information is the ϵ_x deformation directly under the gate. For the DFEH experiments, this information can be lost in projection as the

specimen is rotated around the [1 1 0] axis. A 2° specimen tilt in a 150 nm thick specimen will impose a 5.25 nm limit on the spatial resolution. The large probe used in NBED also limits the spatial resolution. In principal, the HAADF STEM results shown here have excellent spatial resolution, but the experimental noise makes it necessary to average the measured values over a large area which limits the real spatial resolution. Here the best technique for measuring the deformation directly under the gate is N-PED due to the combination of spatial resolution and precision.

For the CESL device where low values of strain are measured, HAADF STEM can not provide reliable measurements of the deformation due to noise. The use of NBED is problematic as artefacts in the diffraction spots can dominate the signal. DFEH can be used to provide maps of the deformation easily, although the problems with specimen tilt remain. Again N-PED is well adapted for these types of measurements except that for here the specimens were examined on the [0 0 1] zone axis and a higher than usual precession angle was required in order to excite the diffraction spots of interest, thus the spatial resolution here was in the range of 5 nm.

The SOI devices were selected as the region of interest and the reference are at slightly different orientations which leads to problems in seeing both regions when using the dark field mode that is required for DFEH. These devices are also extremely small with the regions of interest often in the range 2–10 nm which means that spatial resolution here is key. HAADF STEM although having poor precision is a powerful technique here as it can be used to quickly measure the deformation from a single image acquired on a zone axis. N-PED is not sensitive to the miscut and in principal has the
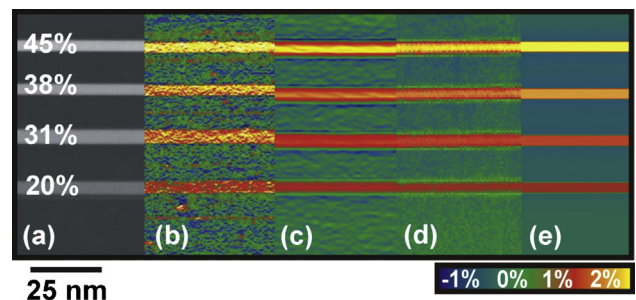

Fig. 19. (a) HAADF STEM image of a calibration specimen used for these experiments (b) ϵ_x deformation map acquired using HAADF STEM (c) DFEH, (d) N-PED and (e) finite element simulations.

Table 2
Comparison of different deformation mapping techniques performed on FEI Titan electron microscopes operated at 200 kV.

	DFEH	NBED	N-PED	HAADF STEM
Spatial resolution	4–6 nm	6 nm	2–5 nm	1–5 nm
Precision	0.02–0.05%	0.1%	0.02–0.05%	0.2–0.4%
Mapping	10–60 s	10–60 min	10–60 min	10–60 s
Field of view	1 μm	Unlimited	Unlimited	200 nm
On zone axis	No	Yes	Yes	Yes
Special equipment	Stable biprism	3rd condensor lens	Precession	Stable microscope
Reference	Close to ROI	Anywhere	Anywhere	Close to ROI
Data processing	Quick (On-line)	Slow (Off-line)	Slow (Off-line)	Quick (On-line)
Advantages	Rapid and precise maps	Simple	Best precision	Best spatial resolution
Problems	Need perfect specimen	Inaccurate results	Data processing long	Poor precision

spatial resolution to perform these measurements easily, however the instabilities of the specimen stages can mean that it can be time consuming waiting for the specimen to stabilise for large and detailed acquisitions. NBED does not have the spatial resolution to easily measure the deformation in these devices, but on the other hand it is not sensitive to mis-orientations between the reference and the region of interest. DFEH is difficult to perform when there is a mis-orientation between the region of interest and the reference as it is not possible to excite both regions simultaneously. DFEH can also provide incorrect results when there is a large mis-orientation between the region of interest and reference. In addition, the spatial resolution caused by specimen tilt is a serious drawback for these small devices.

The superlattice was chosen to give an example of a sample not having perfect crystallographic quality. Here it can be seen that NBED and N-PED measure only the averaged information about the lattice planes projected through the specimen. In addition, the reference can be selected from the region of highest crystalline quality. The HAADF STEM images are poor quality when recording regions where the lattice has many defects and thus the GPA algorithm does not work well. The phases measured by DFEH are extremely sensitive to dislocations and defects and thus the deformation measured in these regions can be complicated to interpret, especially in cases of high densities of dislocations and/or if the spatial resolution delocalises this information. In addition, it is necessary to have a perfect reference next to the region of interest which is not always the case when examining complex semiconductor materials.

There are many other types of specimens which have not been considered here, these include nano wires which have successfully been examined by both NBED (Taraci et al., 2005; Béché et al., 2011) and STEM imaging (Larsson et al., 2007). The deformation in Graphene has been examined using high-resolution TEM images (Young et al., 2011). The main problem with quantum dots is their small size and thus typically these are examined using high resolution TEM or STEM images, however DFEH has been successfully been applied to these types of specimens using special lens settings to provide both a large field of view and a spatial resolution of 1 nm, in this case an entire quantum dot was encapsulated in a 35-nm-thick specimen which reduced the effect of specimen tilting (Cooper et al., 2011b).

4.2. Comparison of the different techniques

This manuscript discussed the current state-of-the-art for deformation mapping using a range of recently developed TEM-based techniques. A non-exhaustive summary of the advantages and disadvantages of all of the different techniques is shown in Table 2.

DFEH has excellent precision in perfect specimens that are grown by epitaxy. The precision can be further improved by using modern microscopes with high brightness sources or by adding many holograms together. However, the quality of the specimen tends to limit the experimental precision. Using standard lens settings, the field of view is in the range 200–500 nm for the best precision, however this can be extended to a micron or even tens of microns using special microscope lens settings. In Table 2 a value of 4–6 nm has been given for the spatial resolution as this is representative of published results. In principal, electron holography can achieve sub-angstrom resolution for small fields of view (Lichte et al., 2008) and by using modern electron microscopes this is straightforward to achieve (Cooper et al., 2014b). However, a serious problem for DFEH which may not have a solution is the need to tilt the specimen from a zone axis, however, this can be minimised by examining thinner specimens at the expense of thin foil relaxation and bending. Where DFEH excels is for the speed of both the data acquisition and processing and deformation maps can be updated every few seconds for dynamic mapping. However, the specimen preparation can be time consuming and thus holography is not always the quickest solution for the studies of deformation in devices. At this time, many commercially available biprism systems have poor stability and have variable performance from day to day, as such efforts are required to improve this situation.

NBED today is the workhorse of the semiconductor industry and it has proved itself as a technique that can be used to perform device systematic studies. However, the non-uniform intensity in the spots can provide results that are incorrect and as such NBED is not a robust technique. NBED has been used widely for deformation mapping and although the spatial resolution is poor when compared to the other techniques, it is simple to perform, the specimen is oriented on the zone axis and in the hands of an experienced microscopist who understands the artefacts, can be used to solve many types of materials science problems. The non-uniformity in the spots are the key problem in NBED and these have been solved by precessing the beam which leads to uniform illumination in the diffraction patterns.

N-PED being an extension of NBED has an advantage of using a higher convergence angle can be used to form a smaller probe for improved spatial resolution. Using N-PED in an aberration corrected electron microscope, the electron probe with a convergence angle of 2.4 mrads measured in vacuum is less than 1 nm in diameter which spreads to 1.5 nm when measured on a typical TEM specimen which can increases to more than 2.0 nm when the beam is precessed. The spatial resolution of N-PED is limited by the spreading of the beam in the specimen and the precession angle which is off-axis relative to the specimen. For a 150-nm-thick specimen, the spatial resolution will be 1.3 or 2.6 nm for precession angles of 0.25° and 0.50° respectively.

It is possible to record large quantities of diffraction patterns to produce detailed deformation maps of the specimens. An advantage of using maps instead of profiles is that it is possible to see if the region of the specimen that has been examined is representative of the device as a whole. Today N-PED seems to provide the best combination of spatial resolution, precision and robustness from artefacts. In addition, it is very insensitive to thickness variations in the specimen and thus time consuming preparation techniques such as back side milling are not required. The experiment and processing can take between from a few minutes to several hours

depending on the size of the map acquired. These acquisition times will be significantly improved in the future by using faster and more efficient CCD cameras (Müller et al., 2012b; Özdöl et al., 2015), by optimising the precession parameters of the beam (Mahr et al., 2015) and by the ability to process the data live. Drift correction will also be required for high volumes of deformation measurements as at this time it is necessary to wait for each specimen to stabilise in the stage before starting each experiment. At this time, N-PED is not widely available in electron microscopes using the imaging capabilities of the CCD camera. However, it is possible to use a commercially available off-axis television camera to measure the positions of the diffraction spots for deformation mapping and a precision of 0.03% and 4 nm spatial resolution has been reported on a pre-aberration-corrected generation microscope (Vigouroux et al., 2014).

HAADF STEM is a simple method that can be used to measure deformation with the best spatial resolution. The spatial resolution is imposed by the mask used in Fourier space during GPA analysis and as such it can be varied after the experiment to provide optimised deformation maps. One of the great advantages of using HAADF STEM is that it is rapid in terms of the experiment and the data processing and it does not require any complicated specimen preparation. In all the examples shown here, the precision is poor, even when a state-of-the-art electron probe-corrected microscope, equipped with a high brightness gun is used. The most important factor here is a stable microscope column and STEM scanning engine and the aberration correction is not key. It would also be possible to add a large series of STEM images together to improve the precision. Although the field of view using this approach is relatively small compared to the other techniques, new approaches such as Moire STEM (Kim et al., 2013a,b, 2014b) or revolving STEM (Sang and Le Beau, 2014) are addressing this problem. Indeed Moire STEM has been shown to be a simple and effective method of measuring the deformation in semiconductor devices, however as it is a variation of the HAADF STEM approach the advantages and disadvantages between the two are similar and as such this has not been discussed in detail. An alternative approach to the GPA treatment of HAADF STEM images is the use of peak finding algorithms (Galindo et al., 2007; Guerrero et al., 2009; Grieb et al., 2012; Zuo et al., 2014), however these approaches require the atoms to be well sampled and are heavier regarding the computation of the maps which limits the field of view. HAADF STEM is adapted for systems where large values of deformation are expected and for very small devices such as quantum dots or delta layers.

Not all of the different deformation techniques that are available today have been presented in this paper. The GPA of TEM images is the classic strain mapping technique. However, the contrast in a TEM image is sensitive to specimen thickness and the microscope focus and aberrations and as such this technique works best for the measurement of high values of deformation over very small fields of view even if the specimen is perfectly flat. Additionally, the damaged surface layers that are present on 100-nm-thick FIB prepared specimens are not suited to high-resolution TEM. Convergent beam electron diffraction is a powerful method of measuring the deformation semiconductor materials. For example recently it has been shown that seven of the nine parameters of the deformation tensor can be determined instead of the four that are obtainable in the techniques shown here (Martin et al., 2014). However, data processing is heavy and as such it is unsuitable for the semiconductor industry where often the rapid calculation of maps showing ϵ_x or ϵ_z is adequate. In addition, it is necessary to tilt the specimens to high-order zone axis which has the effect of limiting the types and sizes of device that can be examined. In-line DFEH can be used to measure the deformation in semiconductor materials and has some advantages over DFEH (Koch and Lubk, 2010) in that neither an adjacent reference region or electron biprism are required

(Özdöl et al., 2010, 2014; Song et al., 2015). However, again the data processing involving the use of the transport of intensity equation is more lengthy than for DFEH (Song et al., 2013) and the problem of needing the specimen to be tilted away from a zone axis remains.

5. Conclusion

This manuscript has discussed the advantages and disadvantages of four different deformation mapping techniques that have been developed in the last 10 years for semiconductor development. In this time, we have benefited enormously from the development of the new generations of ultra-stable electron microscopes which allow a range of different techniques to be applied to different specimens during a single TEM session. At CEA LETI, it was originally envisaged that NBED would be used to support the device development activities. At around the same time following the paper of Hytch, DFEH was developed to provide an additional method of quickly and easily providing deformation maps. Both these techniques were quickly found to be insufficient in terms of spatial resolution for many of the modern devices that are under development. Deformation mapping using HAADF STEM was then developed in order to provide the required spatial resolution. HAADF STEM can be used to assess if devices are strained or not, but is not suitable for measuring precise values of the deformation. Thus N-PED for deformation mapping has been recently been the focus of research in order to provide a technique that can provide both the required precision and spatial resolution.

The development of the FIB is key for these studies, the deformation measurements presented here are insensitive to the levels of Ga implantation, the presence of amorphous layers or even the surface defects that are introduced. Thus the FIB can quickly, reliably and reproducibly provide site-specific specimens to perform systematic studies over a long time periods. Although advanced TEM can be used to provide deformation measurements, simulations are required for each different type of specimen examined to see the effects of thin foil relaxation. The small dimensions of the latest generation devices has the effect of limiting the relaxation compared to the larger specimens that were examined 10–15 years ago. However, simulations are still important to assess the relaxation for different types of material and device geometry.

In the last 10 years an incredible amount of progress has been made in terms of deformation mapping which has been driven by the needs of the semiconductor industry. This manuscript has been written to provide a snapshot of what performance can be expected in terms of deformation mapping using a TEM. There are many different techniques available all of which have different advantages and disadvantages and it is important to choose the correct one depending on the capabilities of the available microscopes and for each type of materials system. At this time we are able to answer most of the questions that are posed during device development and are able to measure deformation in the smallest and most complicated device structures such as FinFETs and nanowire based technologies (Nguyen et al., 2014). But more and more we are asked for the deformation in three dimensions. In this paper we have tried to foresee the TEM developments which are required to improve the different techniques, but for sure there will be many surprises and this story is far from over.

References

Armigliato, A., Balboni, R., Carnevale, G.P., Pavia, G., Piccalo, D., Frabboni, S., Benedetti, A., Cullis, A.G., 2003. Application of convergent beam electron diffraction to two-dimensional strain mapping in silicon devices. Appl. Phys. Lett. 98, 082113.

Armigliato, A., Frabboni, S., Gazzadi, G.C., 2008. Electron diffraction with ten nanometer beam size for strain analysis of nanodevices. Appl. Phys. Lett. 93, 161906.

Béché, A., Hartmann, J.-M., Clément, L., Rouvière, J.-L., 2009. Improved precision in strain measurement using nanobeam electron diffraction. Appl. Phys. Lett. 95, 123114.

Béché, A., Bougerol, C., Cooper, D., Daudin, B., Rouvière, J.-L., 2011. Measuring two dimensional strain state of AlN quantum dots in GaN nanowires by nanobeam electron diffraction. J. Phys.: Conf. Ser. 326, 012047, IOP Publishing.

Béché, A., Rouvière, J.-L., Barnes, J.P., Cooper, D., 2013. Strain measurement at the nanoscale: comparison between convergent beam electron diffraction, nanobeam electron diffraction, high resolution imaging and dark field electron holography. Ultramicroscopy 131, 10.

Baumann, F.H., 2014. High precision two-dimensional strain mapping in semiconductor devices using nanobeam electron diffraction in the transmission electron microscope. Appl. Phys. Lett. 104, 262102.

Braidy, N., Le Bouar, Y., Lazar, S., Ricolleau, C., 2012. Correcting scanning instabilities from images of periodic structures. Ultramicroscopy 118, 67–76.

Bruel, M., 1995. Silicon on insulator material technology. Electron. Lett. 31, 1201–1202.

Boureau, V., Benoit, B., Warot, B., Htch, M., Claverie, A., 2015. Strain/composition interplay in thin SiGe layers on insulator processed by Ge condensation. Mater. Sci. Semicond. Proc., http://dx.doi.org/10.1016/j.mssp.2015.07.034.

Catalan, G., Seidel, J., Ramesh, R., Scott, J.F., 2012. Domain wall nano-electronics. Rev. Mod. Phys. 84, 119.

Chen, L.-C., Chen, F.-R., Kai, J.J., Chang, L., Ho, J.-K., Jong, C.-S., Chiu, C.-C., Chien, C., Huang, C.-N., Chen, C.-Y., Shih, K.-K., 1999. Microstructural investigation of oxidized Ni/Au Ohmic contact to p-type GaN. J. Appl. Phys. 86, 3826–3832.

Cherkashin, N., Reboh, S., Lubk, A., Hytch, M., Claverie, A., 2013. Strain in hydrogen-implanted Si investigated using dark field electron holography. Appl. Phys. Exp. 6, 091301.

Cherns, D., Jiao, C.G., 2001. Electron holography studies of the charge on dislocations in GaN. Phys. Rev. Lett. 87, 205504.

Chu, M., Sun, Y., Aghoram, U., Thompson, S.E., 2009. Strain: a solution for higher carrier mobility in nanoscale MOSFETs. Ann. Rev. 39, 203.

Chung, J., Lian, G., Rabenberg, L., 2010. Practical and reproducible mapping of strains in Si devices using geometric phase analysis of annular dark-field images from scanning transmission electron microscopy. IEEE Electron. Dev. 31, 854.

Clement, L., Pantel, R., Kwakman, L.F.Tz., Rouvière, J.-L., 2004. Strain measurements by convergent-beam electron diffraction: the importance of stress relaxation in lamelle preparations. Appl. Phys. Lett. 85, 651–653.

Cooper, D., Ailliot, C., Truche, R., Hartmann, J., Barnes, J.-P., Bertin, F., Chabli, A., 2008. Medium resolution electron holography with milliVolt sensitivity. J. Appl. Phys. 104, 064513.

Cooper, D., Béché, A., Hartmann, J.-M., Barnes, J.-P., Rouvière, J.-L., 2009. Dark field electron holography for quantitative strain measurements with nanometer-scale spatial resolution. Appl. Phys. Lett. 95, 053501.

Cooper, D., Béché, A., Hartmann, J.-M., Carron, V., Rouvière, J.-L., 2010a. Strain evolution during the silicidation of nanometer-scale SiGe semiconductor devices studied by dark field electron holography. Appl. Phys. Lett. 96, 113508.

Cooper, D., Béché, A., Hartmann, J.-M., Carron, V., Rouvière, J.-L., 2010b. Strain mapping for the semiconductor industry by dark-field electron holography and nanobeam electron diffraction with nm resolution. Semicond. Sci. Technol. 25, 095012.

Cooper, D., de la Pena, F., Béché, A., Rouvière, J.-L., Servanton, G., Pantel, R., Morin, P., 2011a. Field mapping with nanometer-scale resolution for the next generation of electronic devices. Nano Lett. 11, 4585–4590.

Cooper, D., Rouvière, J.-L., Béché, A., Kadkhodazadeh, S., Semenova, E., Yvind, K., Dunin-Borkowski, R.E., 2011b. Quantitative strain mapping of InAs/InP quantum dots with 1 nm spatial resolution using dark field electron holography. Appl. Phys. Lett. 99, 261911.

Cooper, D., Denneulin, T., Barnes, J.-P., Hartmann, J.-M., Hutin, L., LeRoyer, C., Rouvière, J.-L., 2012a. Strain mapping with nm-scale resolution for the silicon-on-insulator generation of semiconductor devices by advanced electron microscopy. J. Appl. Phys. 112, 124505.

Cooper, D., LeRoyer, C., Béché, A., Rouvière, J.-L., 2012b. Strain mapping for the silicon-on-insulator generation of semiconductor devices by high-angle annular dark field scanning electron transmission microscopy. Appl. Phys. Lett. 100, 233121.

Cooper, D., Rivallin, P., Guegan, G., Plantier, C., Robin, E., Guyot, F., Constant, I., 2014a. Field mapping of focused ion beam prepared semiconductor devices by off-axis and dark field electron holography. Semicond. Sci. Technol. 28, 125013.

Cooper, D., Pan, C.T., Haigh, S., 2014b. Atomic resolution electrostatic potential mapping of grapheme sheets by off-axis electron holography. J. Appl. Phys. 115, 223709.

Cooper, D., Bernier, N., Rouvière, J.-L., 2015. Combining 2 nm spatial resolution and 0.02% precision for deformation mapping of semiconductor specimens in a transmission electron microscope by precession electron diffraction. Nano Lett. 15, 5289–5294.

Denneulin, T., Cooper, D., Béché, A., Hartmann, J.-M., Rouvière, J.-L., 2012. The addition of strain in uniaxially strained transistors by both SiN contact etch stop layers and recessed SiGe sources and drains. J. Appl. Phys. 112, 094314.

Denneulin, T., Cooper, D., Rouvière, J.-L., 2014. Practical aspects of strain measurement in thin SiGe layers by (0 0 4) dark-field electron holography in Lorentz mode. Micron 62, 52–65.

Diercks, D., Lian, G., Chung, J., Kaufman, M., 2011. Comparison of convergent beam electron diffraction and geometric phase analysis for strain measurement in a strained silicon device. J. Microsc. 241, 195–199.

Eneman, G., Verheyen, P., De Keersgieter, A., Jurczack, M., De Meyer, K., 2007. Scalability of stress induced by contact etch stop layers: a simulation study. IEEE Trans. Electron. Dev. 54, 1446–1452.

Favia, P., Popovici, M., Eneman, G., Wang, G., Bargallo-Gonzalez, M., Simoen, E., Menou, N., Bender, H., 2010. Nano-beam diffraction: crystal structure and strain analysis at the nanoscale. ECS Trans. 33, 205–219.

Favia, P., Gonzales, M., Bargallo, M., Simoen, E., Verheyen, P., Klenov, D., Bender, H., 2011. Nanobeam diffraction: technique evaluation and strain measurement on complementary metal oxide semiconductor devices. J. Electrochem. Soc. 158 (4), H438–H446.

Galindo, P.L., Kret, S., Sanchez, A.M., Laval, J.-Y., Yáñez, A., Pizarro, J., Guerrero, E., Ben, T., Molina, S.I., 2007. The Peak Pairs algorithm for strain mapping from HRTEM images. Ultramicroscopy 107, 1186–1193.

Gibson, J.M., Treacy, M.M.J., 1984. The effect of elastic relaxation on the local structure of lattice-modulated thin films. Ultramicroscopy 14, 345.

Gouyé, A., Hue, F., Halimaoui, A., Kermarrec, O., Campidelli, Y., Hytch, M., Houdellier, F., Claverie, A., Bensahel, D., 2009. Selective growth of tensely strained SiC films on patterned Si substrates. Mater. Sci. Semicond. Proc. 12, 34–39.

Grieb, T., Müller, K., Fritz, R., Schowalter, M., Neugebohrn, N., Knaub, N., Volz, K., Rosenauer, A., 2012. Determination of the chemical composition of GaNAs using STEM HAADF imaging and STEM strain state analysis. Ultramicroscopy 117, 15–23.

Guerrero, E., Galindo, P.L., Yáñez, A., Pizarro, J., Guerrero-Lebrero, M.P., Molina, S.I., 2009. Accuracy assessment of strain mapping from Z-contrast images of strained nanostructures. Appl. Phys. Lett. 95, 143126.

Hähnel, A., Reiche, M., Moutanabbir, O., Blumtritt, H., Geisler, H., Hoentschel, J., Engelmann, H.J., 2011. Nanobeam electron diffraction evaluation of strain behaviour in nano-scale patterned strained silicon-on-insulator. Phys. Stat. Sol. (c) 8, 1319–1324.

Hähnel, A., Reiche, M., Moutanabbir, O., Blumtritt, H., Geisler, H., Höntschel, J., Engelmann, H.J., 2012. Improving accuracy and precision of strain analysis by energy-filtered nanobeam electron diffraction. Microsc. Microanal. 18, 229–240.

Hanszen, K.J., 1986. Method of off-axis electron holography and investigations of the phase structure in crystals. J. Phys. D 19, 373.

Harscher, A., Lichte, H., 1986. Experimental study of amplitude and phase detection limits in electron holography. Ultramicroscopy 64, 57–66.

Hosseini-Vargargah, S., Couillard, M., Cui, K., Ghanad Tavakoli, S., Robinson, B., Kleiman, R.N., Preston, J.S., Botton, G., 2011. Strain relief and AlSb buffer layer morphology in GaSb heteroepitaxial films grown on Si as revealed by high-angle annular dark-field scanning transmission electron microscopy. Appl. Phys. Lett. 98, 082113.

Houdellier, F., Jacob, D., Casanove, M.J., Roucau, C., 2008. Effect of sample bending on diffracted intensities observed in CBED patterns of plan view strained samples. Ultramicroscopy 108, 295–301.

Huang, J., Kim, M.J., Chidambaram, P.R., Irwin, R.B., Jones, P.J., Weijtmans, J.W., Koontz, E.M., Wang, Y.G., Tang, S., Wise, S., 2006. Probing nanoscale local lattice strains in advanced Si complementary metal-oxide-semiconductor devices. Appl. Phys. Lett. 89, 063114.

Hue, F., Hytch, M., Houdellier, F., Snoeck, E., Claverie, A., 2008a. Strain mapping in MOSFETS by high-resolution electron microscopy and electron holography. Mater. Sci. Eng. B 154, 221–224.

Hue, F., Hytch, M., Bender, H., Houdellier, F., Claverie, A., 2008b. Direct mapping of strain in a strained silicon transistor by high-resolution electron microscopy. Phys. Rev. Lett. 100, 156602.

Hue, F., Hytch, M., Houdellier, F., Bender, H., Claverie, A., 2009. Strain mapping of tensely strained silicon transistors with embedded SiC source and darin by dark field electron holography. Appl. Phys. Lett. 95, 073103.

Hytch, M., Snoeck, E., Kilaas, R., 1998. Quantitative measurement of displacement and strain fields from HREM micrographs. Ultramicroscopy 74, 131.

Hytch, M., Plamann, T., 2001. Imaging conditions for reliable measurement of displacement and strain in high-resolution electron microscopy. Ultramicroscopy 87, 199–212.

Hytch, M., Houdellier, F., Hue, F., Snoeck, E., 2008. Nanoscale holographic interferometry for strain measurements in electronic devices. Nature 453, 1086.

Hytch, M., Cherkashin, N., Reboh, S., Houdellier, F., Claverie, A., 2011. Strain mapping in layers and devices by electron holography. Phys. Stat. Sol. (a) 208, 580–583.

Johnson, C.L., Snoeck, E., Ezcurdia, M., Rodríguez-González, B., Pastoriza-Santos, I., Liz-Marzán, L.M., Hytch, M., 2007. Effects of elastic anisotropy on strain distributions in decahedral gold nanoparticles. Nat. Mater. 7, 120–124.

Jones, E., Cooper, D., Rouvière, J.-L., Béché, A., Azize, M., Palacios, T., Gradecak, S., 2013. Towards rapid nanoscale measurement of strain in III-nitride heterostructures. Appl. Phys. Lett. 103, 231904.

Jones, N., Nellist, P., 2013. Identifying and correcting scan noise and drift in the scanning transmission electron microscope. Microsc. Microanal. 19, 1050–1060.

Jouneau, P.H., Tardot, A., Feuillet, G., Mariette, H., Cibert, J., 1994. Strain mapping of ultra-thin epitaxial ZnTe and MnTe layers embedded in CdTe. J. Appl. Phys. 75, 7310–7316.

Kim, M., Zuo, J.M., Park, G.-S., 2004. High-resolution strain measurement in shallow trench isolation structures using dynamic electron diffraction. Appl. Phys. Lett. 84, 2181–2183.

Kim, S., Kondo, Y., Lee, K., Byun, G., Kim, J.-J., Lee, S., Lee, K., 2013a. Quantitative measurement of strain field in strained-channel-transistor arrays by scanning Moiré fringe imaging. Appl. Phys. Lett. 103, 033523.

Kim, S., Lee, S., Oshima, Y., Kondo, Y., Okunishi, E., Endo, N., Jung, J., Byun, G., Lee, S., Lee, K., 2013b. Scanning Moiré fringe imaging for quantitative strain mapping in semiconductor devices. Appl. Phys. Lett. 102, 161604.

Kim, S., Byeon, D.-S., Jang, H., Koo, S.-M., Lee, H.-J., Ko, D.-H., 2014a. Strain characterization of fin-shaped field effect transistors with SiGe stressors using nanobeam electron diffraction. Appl. Phys. Lett. 105, 083104.

Kim, S., Jung, Y., Kim, J.-J., Byun, G., Lee, S., Lee, H., 2014b. Direct observation of nanometer-scale strain field around $CoSi_2$/Si interface using scanning Moiré fringe imaging. Appl. Phys. Lett. 104, 161610.

Koch, C.T., Lubk, A., 2010. Off-axis and inline electron holography: a quantitative comparison. Ultramicroscopy 110, 460–471.

Koch, C.T., Özdöl, V.B., van Aken, P., 2010b. An efficient, simple, and precise way to map strain with nanometer resolution in semiconductor devices. Appl. Phys. Lett. 96, 091901.

Larsson, M.W., Wagner, J.B., Wallin, M., Håkansson, P., Fröberg, L.E., Samuelson, L., Wallenberg, L.R., 2007. Strain mapping in free-standing heterostructured wurtzite InAs/InP nanowires. Nanotechnology 18, 015504.

Leith, E.N., Upatnieks, J., 1962. Reconstructed waterfronts and communication theory. J. Optic. Soc. Am. 52, 1123–1130.

Lichte, H., Formanek, P., Lenk, A., Linck, M., Matzeck, C., Lehmann, M., Simon, P., 2008. Electron holography – basics and applications. Ann. Rev. Mater. Res. 37, 539–588.

Lubk, A., Javon, E., Cherkashin, N., Reboh, S., Gatel, C., Hytch, M.J., 2014. Dynamic scattering theory for dark-field electron holography of 3D strain fields. Ultramicroscopy 136, 42.

Mahr, C., Müller, K., Grieb, T., Schowalter, M., Merthens, T., Kruse, F., Zillman, D., Rosenauer, A., 2015. Theoretical study of precision and accuracy of strain analysis by nano beam electron diffraction. Ultramicroscopy 158, 38–48.

Martin, Y., Rouvière, J.-L., Zuo, J.M., Favre-Nicolin, V., 2014. Towards a full retrieval of the deformation tensor *F* using convergent beam electron diffraction. Ultramicroscopy, http://dx.doi.org/10.1016/j.ultramic.2014.12.009.

McCartney, M.R., Smith, D.J., 2008. Electron holography: phase imaging with nanometer resolution. Ann. Rev. Mater. Res. 37, 729–767.

McLeod, R.A., Bergen, M., Malec, M., 2014. Phase measurement error in summation of electron holography series. Ultramicroscopy 141, 38–50.

Miao, J., Charalambous, P., Kirz, J., Sayre, D., 1999. Extending the methodology of X-ray crystallography to allow imaging of micrometre-sized non-crystalline specimens. Nature 400, 342–344.

Morvan, S., Le Royer, C., Andrieu, F., Perreau, P., Morand, Y., Cooper, D., Casse, M., Garros, X., Hartmann, J.-M., Tosti, L., Brvard, L., Ponthenier, F., Rivoire, M., Euvrard, C., Seignard, A., Besson, P., Caubet, P., Leroux, C., Gassilloud, R., Saidi, B., Allain, F., Tabone, C., Poiroux, T., Faynot, O., 2013. Gate-last integration on planar FDSOIMOSFET: impact of mechanical boosters and channel orientations. In: International Electron Devices Meeting (IEDM), Washington, DC, 9–11 December.

Müller, K., Rosenauer, A., Schowalter, M., Zweck, J., Fritz, R., Volz, K., 2012a. Strain Measurement in semiconductor heterostructures by scanning transmission electron microscopy. Microsc. Microanal. 18, 995–1009.

Müller, K., Ryll, H., Ordavo, I., Ihle, S., Struder, L., Volz, K., Zweck, J., Soltau, H., Rosenauer, A., 2012b. Scanning transmission electron microscopy strain measurement from millisecond frames of a direct electron charge coupled device. Appl. Phys. Lett. 101, 212110.

Naito, M., Ishimaru, M., Hirotsu, Y., Takashima, M., 2004. Local structure analysis of Ge–Sb–Te phase change materials using high-resolution electron microscopy and nanobeam diffraction. J. Appl. Phys. 95, 8130–8135.

Nguyen, P., Barraud, S., Tabone, C., Gaben, L., Casse, M., Glowacki, F., Hartmann, J.-M., Samson, M.-P., Maffini-Alvaro, V., Vizioz, C., Bernier, N., Guedj, C., Mounet, C., Rozeau, O., Toffoli, A., Alain, F., Delprat, D., Nguyen, B.-Y., Mazure, C., Faynot, O., Vinet, M., 2014. Dual-channel CMOS co-integration with Si NFET and strained-SiGe PFET in nanowire device architecture featuring sub-15nm gate length. In: International Electron Devices Meeting (IEDM), San Francisco, 15–17 December.

Okamoto, H., Hokazono, A., Adachi, K., Yasutake, N., Itokawa, H., Okamoto, S., Kondo, M., Tsujii, H., Ishida, T., Aoki, N., 2008. In situ doped embedded-SiGe source/drain technique for 32 nm node p-channel metal-oxide-semiconductor field-effect transistor. Jap. J. Appl. Phys. 47, 2564.

Overwijk, M.H.F., van den Heuvel, F.C., Bulle-Lieuwma, C.W.T., 1993. Novel scheme for the preparation of transmission electron microscopy specimens with a focused ion beam. J. Vac. Sci. Technol. B 11, 2021.

Özdöl, V.B., Koch, C.T., van Aken, P.A., 2010. A non-damaging electron microscopy approach to map In distribution in InGaN light-emitting diodes. J. Appl. Phys. 108, 056103.

Özdöl, V.B., Tyutyunnikov, D., Koch, C.T., van Aken, P.A., 2014. Strain mapping for advanced CMOS technologies. Cryst. Res. Technol. 49, 38–42.

Özdöl, V.B., Gammer, C., Lin, X.G., Ercius, P., Orphus, C., Ciston, J., Minor, A.M., 2015. Strain mapping at nanometer resolution using advanced nano-beam electron diffraction. Appl. Phys. Lett. 106, 253107.

Reboh, S., Benzo, P., Morin, P., Cours, R., Hytch, M.J., Claverie, A., 2013a. A method to determine the Young's modulus of thin-film elements assisted by dark-field electron holography. Appl. Phys. Lett. 102, 051911.

Reboh, S., Morin, P., Hytch, M.J., Houdellier, F., Clavierie, A., 2013b. Mechanics of silicon nitride thin-film stressors on a transistor-like geometry. APL Mater. 1, 042117.

Rosenauer, A., Remmele, T., Gerthsen, D., Tillmann, K., Förster, A., 1997a. Atomic scale strain measurements by the digital analysis of transmission electron microscopic lattice images. Optik 105, 99–107.

Rosenauer, A., Fischer, U., Gerthsen, D., Förster, F., 1997b. Composition evaluation of InGaAs Stranski–Krastanow island structures by strain state analysis. Appl. Phys. Lett. 71, 3868–3870.

Rosenauer, A., Gerthsen, D., Potin, V., 2006. Strain state analysis of InGaN/GaN sources of error and optimized imaging conditions. Phys. Stat. Sol. (a) 203, 176–184.

Rouvière, J.-L., Sarigiannidou, E., 2006. Theoretical discussions on the geometrical phase analysis. Ultramicroscopy 106, 1.

Rouvière, J.-L., Béché, A., Martin, Y., Denneulin, T., Cooper, D., 2013. Improved strain precision with high spatial resolution using nanobeam precession electron diffraction. Appl. Phys. Lett. 103, 241913.

Sands, T., 1987. Stability and epitaxy if NiAl and related inter metallic films on III–V compound semiconductors. Appl. Phys. Lett. 52, 197.

Sang, X., Le Beau, J., 2014. Revolving scanning transmission electron microscopy: correcting sample drift distortion without prior knowledge. Ultramicroscopy 138, 28–35.

Sarigiannidou, E., Monroy, E., Daudin, B., Rouvière, J.-L, Andreev, A.D., 2005. Strain distribution in GaN–AlN quantum-dot superlattices. Appl. Phys. Lett. 87, 203112.

Sato, T., Matsumoto, H., Nakano, K., Konno, M., Fukui, M., Nagaoki, I., Taniguchi, Y., 2010. Application of lattice strain analysis of semiconductor device by nanobeam diffraction using the 300 kV cold-FE TEM. J. Phys.: Conf. Ser., 241, IOP Publishing.

Schlom, D.G., Chen, L.Q., Eom, C.B., Rabe, K.M., Streiffer, S.K., Triscone, J.M., 2007. Strain tuning of ferroelectric thin films. Ann. Rev. 37, 589.

Seitz, H., Seibt, M., Baumann, F.H., Ahlborn, K., Schröter, W., 1995. Quantitative strain mapping using high-resolution electron microscopy. Phys. Stat. Sol. (a) 150, 625–634.

Senez, V., Armigliato, A., de Wolf, I., Carnevale, G., Balboni, R., Frabboni, S., Benedetti, A., 2003. Strain determination in silicon microstructures by convergent beam electron diffraction, process simulation and micro-Raman spectroscopy. J. Appl. Phys. 94, 5574.

Sickmann, J., Formanek, P., Linck, M., Muehle, U., Lichte, H., 2011. Imaging modes for potential mapping in semiconductor devices by electron holography with improved lateral resolution. Ultramicroscopy 111, 290–302.

Song, K., Shin, G.-Y., Kim, J.-K., Oh, S.-H., Koch, C.T., 2013. Strain mapping of LED devices by dark-field inline electron holography: comparison between deterministic and iterative phase retrieval approaches. Ultramicroscopy 127, 119–125.

Song, K., Koch, C.T., Lee, J.-K., Kim, D.-Y., Kim, J.-K., Parvizi, A., Jung, W.-Y., Park, C.-G., Jeong, H.-J., Kim, H.-S., Cao, Y., Yang, T., Chen, L.-Q., Oh, S.-H., 2015. Correlative high-resolution mapping of strain and charge density in a strained piezoelectric multilayer. Adv. Mater. Interfaces 2, 1400281.

Stier, O., Grundmann, M., Bimberg, D., 1999. Electronic and optical properties of strained quantum dots modelled by 8-band k.p theory. Phys. Rev. B 59, 5688.

Takeguchi, M., McCartney, M.R., Smith, D.J., 2004. Mapping In concentration, strain, and internal electric field in InGaN/GaN quantum well structure. Appl. Phys. Lett. 84, 2103–2105.

Taraci, J.L., Hytch, M., Clement, T., Peralta, P., McCartney, M.R., Drucker, J., Picraux, S.T., 2005. Strain mapping in nanowires. Nanotechnology 16, 2365.

Toda, A., Nakamura, H., Fukai, T., Ikarashi, N., 2008. Channel strain in advanced complementary metal-oxide-semiconductor field effect transistors measured using nano-beam electron diffraction. Jap. J. Appl. Phys. 47, 2496.

Tonomura, A., 1987. Applications of electron holography. Rev. Mod. Phys. 59, 639–669.

Uesugi, F., Akira, H., Shiro, T., 2011. Evaluation of two-dimensional strain distribution by STEM/NBD. Ultramicroscopy 111, 995–998.

Usada, K., Numata, T., Irisawa, T., Hiritasha, N., Takagi, S., 2005. Strain characterization in SOI and strained-Si on SGOI MOSFET channel using nano-beam electron diffraction (NBD). Mater. Sci. Eng. 124, 143.

Vigouroux, M., Delaye, V., Bernier, N., Cipro, R., Lafond, D., Audoit, G., Baron, T., Bertin, F., 2014. Strain mapping at the nanoscale using precession electron diffraction in transmission electron microscope with off axis camera. Appl. Phys. Lett. 105, 191906.

Vincent, R., Midgley, P.A., 1994. Double conical beam-rocking system for measurement of integrated electron diffraction intensities. Ultramicroscopy 53, 271–282.

Voelkl, E., Tang, D., 2010. Approaching routine $2\pi/1000$ phase resolution for off-axis electron holography. Ultramicroscopy 110, 447–459.

Wang, Y.Y., Kawasaki, M., Bruley, J., Gribelyuk, M., Domenicucci, A., Gaudiello, J., 2004. Off-axis electron holography with a dual-lens imaging system and its usefulness in 2-D potential mapping of semiconductor devices. Ultramicroscopy 101, 63–72.

Wang, Y.Y., Bruley, J., van Meer, H., Li, J., Domenicucci, A., Murray, C.E., Rouvière, J.-L., 2013. Strain mapping of Si devices with stress memorization processing. Appl. Phys. Lett. 103, 052104.

Wang, Y.Y., Cooper, D., Rouvière, J.-L., Murray, C.E., Bernier, N., Bruley, J., 2015. Nanoscale strain distributions in embedded SiGe semiconductor devices revealed by precession electron diffraction and dual lens dark field electron holography. Appl. Phys. Lett. 106, 042104.

Weber, O., Josse, E., Andrieu, F., Cros, A., Richard, E., Perreau, P., Baylac, E., Degors, N., Gallon, C., Perrin, E., Chhun, S., Petitprez, E., Delmedico, S., Simon, J., Druais, G., Lasserre, S., Mazurier, J., Guillot, N., Bernard, E., Bianchini, R., Parmigiani, L., Gerard, X., Pribat, C., Gourhant, O., Abbate, F., Gaumer, C., Beugin, V., Gouraud, P., Maury, P., Lagrasta, S., Barge, D., Loubet, N., Beneyton, R., Benoit, D., Zoll, S., Chapon, J.-D., Babaud, L., Bidaud, M., Gregoire, M., Monget, C., Le-Gratiet, B., Brun, P., Mellier, M., Pofelski, A., Clement, L.R., Bingert, R., Puget, S., Kruck, J.-F., Hoguet, D., Scheer, P., Poiroux, T., Manceau, J.-P., Rafik, M., Rideau, D., Jaud, M.-A., Lacord, J., Monsieur, F., Grenouillet, L., Vinet, M., Liu, Q., Doris, B., Celik, M., Fetterolf, S.P., Faynot, O., Haond, M., 2014. 14 nm FDSOI technology for high speed and energy efficient applications. In: VLSI Technology: Digest of Technical Papers, 2014 Symposium, pp. 1–2.

Young, R.J., Gong, L., Kinloch, I.A., Riaz, I., Jalil, R., Novoselov, K.S., 2011. Strain mapping in a graphene monolayer nanocomposite. ACS Nano 5, 3079–3084.

Zhang, P., Istratov, A., Weber, E.R., Kisielowski, C., He, H., Nelson, C., Spence, J.C.H., 2006. Direct strain measurement in a 65nm node strained silicon transistor by convergent-beam electron diffraction. Appl. Phys. Lett. 89, 161907.

Zuo, J.M., Shah, A.B., Kim, H., Meng, Y., Gao, W., Rouvière, J.-L., 2014. Lattice and strain analysis of atomic resolution Z-contrast images based on template matching. Ultramicroscopy 136, 50–60.